LIBRARY

NAVAL POSTGRADUATE SCHOOL
Monterey, California

THESIS

F2254

A Microstructural Investigation of the Shear Distortions and Energetics of Motions Observed in an Aged High Damping 53Cu-45Mn-2Al Alloy

by

David Michael Farkas

March 1989

Thesis Advisor: Jeff Perkins

Approved for public release; distribution is unlimited

T241909

REPORT DOCUMENTATION PAGE

1a. REPORT SECURITY CLASSIFICATION UNCLASSIFIED	1b. RESTRICTIVE MARKINGS
2a. SECURITY CLASSIFICATION AUTHORITY	3. DISTRIBUTION/AVAILABILITY OF REPORT Approved for public release; distribution is unlimited
2b. DECLASSIFICATION/DOWNGRADING SCHEDULE	
4. PERFORMING ORGANIZATION REPORT NUMBER(S)	5. MONITORING ORGANIZATION REPORT NUMBER(S)
6a. NAME OF PERFORMING ORGANIZATION Naval Postgraduate School 6b. OFFICE SYMBOL (*If applicable*) 69	7a. NAME OF MONITORING ORGANIZATION Naval Postgraduate School
6c. ADDRESS (*City, State, and ZIP Code*) Monterey, CA 93943-5000	7b. ADDRESS (*City, State, and ZIP Code*) Monterey, CA 93943-5000
8a. NAME OF FUNDING/SPONSORING ORGANIZATION 8b. OFFICE SYMBOL (*If applicable*)	9. PROCUREMENT INSTRUMENT IDENTIFICATION NUMBER
8c. ADDRESS (*City, State, and ZIP Code*)	10. SOURCE OF FUNDING NUMBERS PROGRAM ELEMENT NO / PROJECT NO. / TASK NO / WORK UNIT ACCESSION NO.

11. TITLE (*Include Security Classification*)
A Microstructural Investigation of the Shear Distortions and Energetics of Motions Observed in an Aged High Damping 53Cu-45Mn-2Al Alloy

12. PERSONAL AUTHOR(S)
David M. Farkas

13a. TYPE OF REPORT	13b. TIME COVERED	14. DATE OF REPORT (*Year, Month, Day*)	15. PAGE COUNT
Engineer's Thesis	FROM _____ TO _____	1989 March	113

16. SUPPLEMENTARY NOTATION "The views expressed in this thesis are those of the author and do not reflect the official policy or position of the Department of Defense or the U.S. Government"

17. COSATI CODES			18. SUBJECT TERMS (*Continue on reverse if necessary and identify by block number*)
FIELD	GROUP	SUB-GROUP	High Damping, Cu-Mn, Cu-Mn-Al, Tweed Microstructure, Flickering, Image Extinctions, Energetics, Chaotic Activity

19. ABSTRACT (*Continue on reverse if necessary and identify by block number*)

The shear distortions developed upon aging of a 53Cu-45Mn-2Al alloy were studied using transmission electron microscope image extinctions and diffraction spot streak analysis. It was determined that a lattice distortion of {110} planes, in <111> directions developed in the alloy as aging progressed. This matured <111> shear induces a distinct V-shaped contrast which displays dynamic motion under the electron-beam irradiation of TEM examination. Video imaging techniques were applied to this dynamic activity, termed "flickering", to investigate the energetics of the underlying crystalline lattice motion. The real-time behavior at the flicker sites suggests that the underlying mechanism which produces the dynamic contrast change is a gradual crystallographic transition, typical of a second-order phase transition. The flicker contrast motion displayed many of the characteristics of "chaotic vibrations".

20. DISTRIBUTION/AVAILABILITY OF ABSTRACT ☒ UNCLASSIFIED/UNLIMITED ☐ SAME AS RPT ☐ DTIC USERS	21. ABSTRACT SECURITY CLASSIFICATION UNCLASSIFIED
22a. NAME OF RESPONSIBLE INDIVIDUAL Professor Jeff Perkins	22b. TELEPHONE (*Include Area Code*) (408)646-2216 22c. OFFICE SYMBOL 69Ps

DD FORM 1473, 84 MAR — 83 APR edition may be used until exhausted. All other editions are obsolete.

SECURITY CLASSIFICATION OF THIS PAGE

☆ U.S. Government Printing Office 1986—606-24.

Approved for public release: distribution is unlimited.

A Microstructural Investigation of the Shear Distortions and Energetics of Motions Observed in an Aged High Damping 53Cu-45Mn-2Al Alloy

by

David Michael Farkas
Lieutenant Commander, United States Navy
BSME, Purdue University, 1976

Submitted in partial fulfillment of the requirements for the degree of

MASTER OF SCIENCE IN MECHANICAL ENGINEERING

and

MECHANICAL ENGINEER

from the

NAVAL POSTGRADUATE SCHOOL
March 1989

ABSTRACT

The shear distortions developed upon aging of a 53Cu-45Mn-2Al alloy were studied using transmission electron microscope image extinctions and diffraction spot streak analysis. It was determined that a lattice distortion of {110} planes, in <111> directions developed in the alloy as aging progressed. This matured <111> shear induces a distinct V-shaped contrast which displays dynamic motion under the electron-beam irradiation of TEM examination. Video imaging techniques were applied to this dynamic activity, termed "flickering", to investigate the energetics of the underlying crystalline lattice motion. The real-time behavior at the flicker sites suggests that the underlying mechanism which produces the dynamic contrast change is a gradual crystallographic transition, typical of a second-order phase transition. The flicker contrast motion displayed many of the characteristics of "chaotic vibrations".

C.1

TABLE OF CONTENTS

I. INTRODUCTION ---------- 1

A. GENERAL ---------- 1

B. BACKGROUND ---------- 2

C. OBJECTIVES ---------- 14

II. EXPERIMENTAL PROCEDURES ---------- 17

A. SAMPLE PREPARATION AND TEM USE ---------- 17

B. MATHEMATICAL PREDICTION EQUATIONS ---------- 18

C. ANALYSIS OF FLICKER ENERGETICS ---------- 22

III. RESULTS AND DISCUSSION ---------- 29

A. DETERMINATION OF SHEAR DISPLACEMENTS -------- 29

B. ENERGETICS OF FLICKER ACTIVITY ---------- 62

C. TRANSFORMATION MODEL FOR AGED ALLOYS -------- 87

IV. CONCLUSIONS ---------- 92

V. RECOMMENDATIONS FOR FUTURE STUDY ---------- 95

APPENDIX A: CONSTRUCTION OF IMAGE CONVERTER ---------- 96

APPENDIX B: HOW TO VIEW STEREOGRAPHIC IMAGES --------- 98

APPENDIX C: COMPUTER PROGRAMS ---------- 99

LIST OF REFERENCES ---------- 102

INITIAL DISTRIBUTION LIST ---------- 106

ACKNOWLEDGEMENT

I would like to thank Professor Jeff Perkins for his insight, guidance and the direction he provided throughout the course of my research. I am especially grateful for the freedom he allowed me in pursuing the rather abstract idea of "chaos" in a crystalline solid. I would also like to thank Professor Tadayoshi Yamashita for his generous assistance in analyzing the electron microscope photographs. Finally, I want to thank Dr. Kenji Adachi, for showing me how to "drive" the TEM.

I. INTRODUCTION

A. GENERAL

Improved vibration damping and sound quieting of machinery, structures and ship components are goals of the U.S. Navy for the twenty-first century. The standard methods of shock and vibration control include reduction of vibration at the source, component isolation, and reduction of the system response. Until recently, the only methods employed to reduce vibrational energy at the source were to balance moving masses, balance magnetic forces, and through the control of component clearances [Ref. 1]. Recent focus has been on the elimination of vibration and noise by selecting construction materials which absorb and dissipate the energy directly at the source via structural damping [Ref. 2]. Several commercial alloys are available which possess the property of high specific damping capacity, however widespread employment of such alloys has been somewhat limited, awaiting optimization and stabilization of their material properties.

Current research at the Naval Postgraduate School has included a systematic investigation of both macroscopic damping and microscopic structural properties of high damping Cu-Mn based alloys. This thesis is part of the continuing investigation of the microstructural properties of aged Cu-Mn damping alloys.

B. BACKGROUND

1. The Copper-Manganese Alloy System

It is appropriate to begin with a review of the physical metallurgy of the Cu-Mn alloy system. The binary phase diagram presented in Figure 1.1, compiled by Mayes [Ref. 3] is based on the results of various workers [Ref. 4,5,6,7].

The diagram shows a broad high temperature region where alloys of varying composition exist in a homogeneous gamma-phase of face-centered-cubic (FCC) structure. At alloy compositions of approximately 50% by weight Mn and greater, an anti-ferromagnetic ordering occurs upon cooling from intermediate aging temperatures [Ref. 8]. The temperature below which this ordering occurs, known as the Néel temperature (T_N), varies with manganese content.

Accompanying this magnetic transition is a tetragonal distortion of the FCC crystalline matrix to a twinned face-centered-tetragonal (FCT) microstructure [Ref. 9, 10, 11, 12, 13], often termed "quasi-martensitic". The degree of tetragonality is very slight [Ref. 14], and it has been suggested that the FCC-to-FCT transition may be second-order in nature [Ref. 15]. Also depicted on the phase diagram is a metastable miscibility gap, below which a decomposition of the homogeneous matrix occurs [Ref. 4, 5]. Decomposition within the miscibility gap leads to a fine dispersion of Mn-enriched regions (MER's), and complimentary Mn-depleted regions. A spatial composition gradient results which

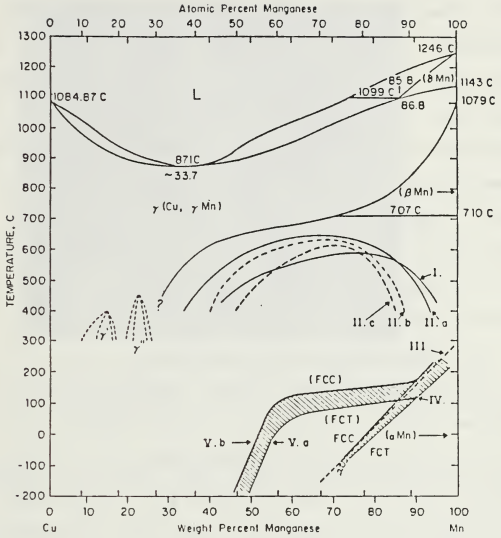

Figure 1.1 The Cu-Mn binary phase diagram showing Miscibility Gap, M_s, and T_N [Ref. 3].
I. Miscibility gap [Ref. 4].
II. Miscibility gap [Ref. 5].
a. Layering range.
b. Chemical Spinodal.
c. Coherent Spinodal.
III. Néel temperature [Ref. 4].
IV. FCC-to-FCT transition in quenched alloy [Ref. 6].
V. FCC-to-FCT transition in aged alloy [Ref. 7].

affects both the local anti-ferromagnetic ordering (T_N) and martensitic phase transition (M_s) start temperatures. Alloys with composition greater that about 82 at. % Mn will be tetragonal at room temperature, while those with Mn content less than this will be cubic at room temperature unless subjected to an intermediate aging treatment. As a result of the composition dependence of M_s, and in order to produce high damping properties with compositions of less than 82 at. % Mn, aging treatments at intermediate temperatures must be employed. (Aging at temperatures in the range of 350°C to 450°C, which are within the miscibility gap, have been investigated.)

2. Tweed Contrast and Flickering

A characteristic "tweed" contrast, visible in transmission electron microscope (TEM) images, develops upon cooling the alloy from the aging temperature. The tweed takes the form of evenly spaced striations (on the order of 10 nm) of bright and dark contrast. The lines of contrast typically form along <110> directions of the parent FCC matrix and display a cross-hatched appearance. The spacing of the tweed striations is sensitive to both aging treatment and to the diffraction conditions. Figure 1.2 displays the tweed contrast from a sample of Cu-Mn-Al alloy aged for 8 hours at 400°C.

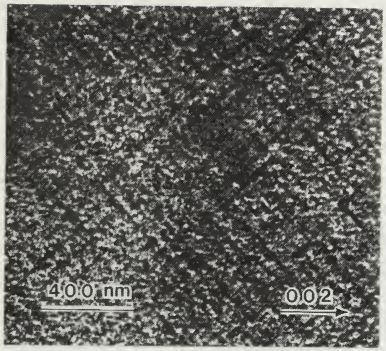

Figure 1.2 Typical tweed contrast observed at short aging times, in this case 8 hours at 400°C. Lines of contrast lie along <110> directions. (100) zone.

Butler and Kelly [Ref. 16], Nittono and coworkers [Ref. 13], and Shimizu and coworkers [Ref. 17] have characterized general tweed microstructures in detail using electron microscopy. The production of tweed contrast requires two basic conditions. First, there must exist a source of finely distributed "centers" of asymmetric strain. Various sources of these strain centers have been identified for different alloy systems and include G-P zones [Ref. 18], finely distributed precipitate particles [Ref. 19], ordered domains [Ref. 20], or simply domains in which there is an incipient

lattice transition that distorts the lattice [Ref. 21]. The second requirement for tweed contrast is the existence of an anisotropic matrix phase. For cubic lattices, certain soft elastic constants will provide the anisotropy necessary for tweed contrast.

The distinct appearance or sharpness of the cross-hatched tweed contrast is quite dependent on the distribution, nature and magnitude of the strain centers, as well as the degree of anisotropy of the matrix phase [Ref. 3]. If any of these factors is deficient, the typical cross-hatched tweed contrast appearance will not appear, and a "mottled" contrast will result. Thus, many "tweedy" alloys show a variation in tweed contrast with changes in the distribution and/or strength of the strain centers [Ref. 18, 22]. This in fact is observed in Cu-Mn based alloys as aging condition or sample temperature is varied.

In Cu-Mn based alloys, aging at intermediate temperatures, leads to spinodal and other decomposition mechanisms, producing phase separation of the alloy into fine regions of Mn-enriched (MER) and Mn-depleted zones. The MER's act as sources of asymmetric strain which render the structure tetragonal and produce the tweed [Ref. 7].

As aging progresses in Cu-Mn alloys, the tweed striations become coarser and less well-defined, and finally yield to characteristic V-shaped or spear images. Relatively longer aging times are necessary for the V-shaped contrast to

appear. For example, aging for 10 hours at 450°C produces a well-defined V-shaped morphology. Figure 1.3 presents a typical micrograph of the V-shaped contrast observed in specimens aged for longer times.

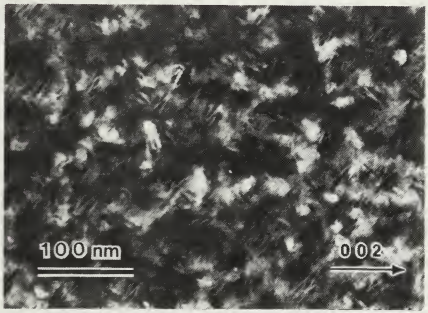

Figure 1.3 Typical V-shaped morphology, with some flickering sites indicated, from a sample pre-aged 10 hours at 450°C to create Mn-enriched regions. (100) zone.

Previous work by Perkins, Mayes, and Yamashita reported the dynamic nature of localized regions of (V-shaped) contrast in aged Cu-Mn alloys [Ref. 23, 24]. The effect was termed "flickering". The size of the regions in which contrast fluctuations were observed was on the order of the

spacing of the tweed diffraction contrast which was also observed, namely 10 to 20 nm. The character of the flickering was described as an observable movement or rotation of lines of contrast at a random frequency varying from about 1 to 10 Hz. It was suggested that the flickering contrast was a manifestation of small sections of the crystal, less than 10 nm in size, flipping a tetragonal distortion from one c-axis orientation to another. This idea is consistent with the development of an array of domains (of appropriate composition) in which the FCC-to-FCT lattice transition becomes favored as aging progresses in the alloy [Ref. 25].

It should be noted that the V-shapes which are noticeable in the photomicrographs presented in this analysis (Figure 1.3 for example) have been obtained from time exposures of regions which contain flickering contrast, and in some cases the contrast will have actually moved during the time of the time exposure.

3. Survey of Other Systems Displaying Dynamic Activity

Structural fluctuations of very small crystals have been reported by other investigators. Several recent papers have dealt with structural changes of small clusters consisting of about 50 to 500 atoms. It is relevant to compare these observations with the flickering activity of aged Cu-Mn alloys, since similarities exist in the size, frequency, morphology, and energy interactions present.

Iijima and Ichihasi (1985) [Ref. 26] reported a continual change of the outer shapes of small FCC metal particles (< 5 nm) when exposed to intense electron-beam irradiation. Accompanying the shape change was a reorganization of the internal atomic arrangement from a single crystal to a twinned crystal and vice versa. The observations suggested that the instabilities of the particles were affected partly by charge fluctuation on the particles or in their vicinity. Often, the formation or annihilation of twin planes and stacking faults triggered the transformation of a particle. The modification in structure took place with cooperative motion of both external and internal atoms. One proposed mechanism of structural modification was via strain-induced Coulomb forces between the particle and substrate.

Smith, Bovin, and colleagues, (1986) [Ref. 27, 28] using high-resolution electron microscopy, observed atomic-level structural rearrangements of small gold crystals (less than 5 nm) supported on thin films of amorphous carbon, silicon, and germanium. The vibrational frequency (estimated at 10 Hz) was dependent on such factors as the particle-substrate contact area, the electrical conductivity of the substrate, and the energy of the incident electron beam, and was found to decrease rapidly as the particle size increased. The changes in crystal structure occurred in conjunction with translational and rotational motion of the particle on the

substrate. Smith surmised that the fluctuations resulted from electron beam heating effects and that the dynamic behavior depended on the thermal contact with the substrate. Dynamic activity resulting from direct kinetic energy transfer from the incident beam was excluded, since structural changes were observed with beam energies below the threshold for exit surface sputtering of gold.

Dundurs, Marks, and Ajayan (1986) [Ref. 29] reported rapid structural fluctuations of FCC particles on the order of 10 nm in size. This shape change of the crystal structure, being fluid-like, was termed "quasi-melting". Further work by these authors (1988) [Ref. 30] presented a theoretical analysis of the energy contributions and of the available energy (during electron-beam interaction) for shape changes. Their work investigated the amount of energy generated during particle-beam interaction and how much of it was available to the particle to overcome the potential energy barrier existing between different shapes. Summarizing their results:

1. Contrary to results obtained by Smith, et al. [Ref. 27, 28] the instability of the microstructure was not caused by the thermal effects of electron-beam heating of the particle. The thermal strain energy was negligible in comparison with surface, internal strain, and surface stress energies.

2. Based on the magnitude of energy variations, the thermal gradients existing in the particles were extremely small (the particles being at almost constant temperature as located on the substrate). The electron-beam irradiation did not significantly heat the particle.
3. By examining the energy differences between various crystal configurations of small particles, the magnitude of the activation barrier between the energetically most unfavorable shapes was estimated to be no more than 10-15 eV. Consideration of the total particle energy as a function of radius indicated that a particle in the size range of 2.5 nm could readily change structure provided that the energy from interaction with the electron beam is on the order of 10-15 eV. A rough estimate indicated that the available energy during electron-beam irradiation was as much as 100-1000 eV.
4. The activation barrier was a strong function of particle size. As particle size increased the activation barrier increased rapidly. (It should be noted that the classical energy of melting of small particles was several orders of magnitude larger.) Experimental observations supported

this, in that for larger particles, the fluctuations were much slower.

Dundurs, et al. [Ref. 30] proposed an electronic excitation phenomenon leading to surface or bulk diffusion (known as Bourgoin-Corbett diffusion) as an explanation for the structural instability. Their model, however, is not considered to be comprehensive and no evidence exists that a particular mechanism is wholly responsible for the phenomena.

Otsuka, Kubo, and Wayman (1981) [Ref. 31] described a time varying effect known as streaming or shimmering in specimens under TEM examination. This effect was observed in several alloys and has been proposed to be a result of mechanical vibration originating from the energy supplied by a gradient of diffuse inelastic scattering occurring at various bend contours within the specimen. Since the effect was observed in numerous alloys, including nontransforming materials, it was concluded that the streaming phenomenon was solely an artifact of the interaction of incident electrons with the thinned specimens.

3. Damping Properties of Aged Cu-Mn Alloys

Many engineering materials display structural damping when excited by mechanical vibration; however most metallic alloys exhibit poor damping capacity at the amplitude of stress associated with vibration and noise emission. The specific damping capacity (SDC) is a quantity used to gage an alloy's degree of structural damping, and is generally quite

low for most materials (i.e. less than 1%). On the other hand, grey cast iron is a common structural metal which is considered to be unusually effective in absorbing vibrational energy. Grey cast iron has a SDC value in the range of 5% to 10%. Several commercially available high damping "quiet" alloys have damping capacities ranging up to 25% to 50%. A high damping material is generally defined as having an SDC greater than 20%. A summary of SDC, yield strength and density is provided in Table 1.1 for various structural materials and damping alloys.

TABLE 1.1

DAMPING CHARACTERISTICS OF SELECTED METALS AT ROOM TEMPERATURE [Ref. 2]

Metal	SDC (%)	Yield Strength (10^3psi)	Density (gm/cm^3)
Magnesium (wrought)	49	26	1.74
Cu-Mn alloys (Incramute, Sonoston)	40	45	7.5
Ni-Ti alloy (Nitinol)	40	25	6.45
Fe-Cr-Al alloy (Silentalloy)	40	40	7.4
High-C gray iron	19	25	7.7
Nickel (pure)	18	9	8.9
Iron (pure)	16	10	7.86
Martensitic stainless steel	8	85	7.7
Gray cast iron	6	25	7.8
SAP (aluminum powder)	5	20	2.55
Low-carbon steel	4	50	7.86
Ferritic stainless steel	3	45	7.75
Malleable, modular cast irons	2	50	7.8
Medium-carbon steels	1	60	7.86
Austenitic stainless steel	1	35	7.8
1100 Aluminum	0.3	5	2.71
Aluminum alloy 2024-T4	<0.2	47	2.77
Nickel-based superalloys	<0.2	30	8.5
Titanium alloys	<0.2	120	4.5
Brasses, bronzes	<0.2	40	8.5

The Cu-Mn alloy system is of interest to the U. S. Navy because of its high damping capacity and its potential marine applications.

The mechanism of damping in Cu-Mn alloys has been the motive of investigation by many researchers. Various views exist as to this energy absorption mechanism. For example, movement of the twin boundaries between FCT plates is a postulated mechanism of damping [Ref. 4, 12, 16]. Hedley proposed that a dual mechanism acts, consisting of a frictional term involving microtwin boundary motion, and energy absorption associated with the reversible rotation of Mn-ion magnetic moments [Ref. 12]. More recently, Mayes and Perkins proposed two additional models, the first of which is directly related to the premartensitic tweed structure which is common in aged alloys, and the second concerning energy absorption by the FCC to FCT transformation as a result of stress induction under vibrational conditions [Ref. 3, 25]. Since SDC of Cu-Mn alloys peaks concurrently with the development of V-shaped contrast, the second of these proposed mechanisms of energy absorption has been the impetus of the current research.

C. OBJECTIVES

The goal of the present research was to develop a broad understanding of the transformations which occur during aging of Cu-Mn based damping alloys, hence the nature of structural

damping mechanisms which are active. Various techniques were employed in this investigation, including analysis of static time-exposed TEM images, and signal processing of dynamic image contrast. These images were analyzed to determine the nature, morphology, and kinetics of development of the underlying structures.

Time-exposed TEM photomicrographs of the dynamic image contrast were analyzed for specimens aged for relatively long times (well beyond that required to create a distinct tweed contrast). The specific techniques which were employed to accomplish this objective included:

1. Systematic use of image extinctions under various diffraction conditions, to determine the direction of the shear distortions which produce the static V-shaped images.
2. Analysis of streaking in selected area diffraction patterns, to identify the morphology of structures developed in the aged alloy.
3. Use of stereographic microphotography, to identify the spatial orientation of the structures present.

The phenomenon of flickering provided a unique opportunity to monitor the reorientation kinetics of the FCT sections of the crystal and thus gain insight into the energy absorption mechanism of damping. By applying video imaging and frequency domain processing of the intensity variations which comprise the flickering contrast observed in TEM images, it was

possible to analyze the energetics and the dynamic nature of the flickering and the underlying crystalline transformation. The objectives of the dynamic signal analysis were:

1. To determine the dependence of flicker frequency on specimen temperature.
2. To correlate the flicker frequency with energy of the TEM beam.
3. To delineate patterns in the time domain variation of flicker activity, e.g. apply techniques of analysis appropriate to complex, non-linear, and chaotic systems.

II. EXPERIMENTAL PROCEDURES

A. SAMPLE PREPARATION AND ELECTRON MICROSCOPE USE

The microscopic images were obtained from samples of a 53.1 wt% Cu - 44.8 wt% Mn - 1.6 wt% Al alloy, originally provided by Olin Metals Research Laboratories in plate form. Samples for TEM examination were obtained by cutting out 3 mm diameter discs, which were hand sanded to a thickness of about 0.3 mm and sealed in evacuated quartz tubes. Heat treatment consisted of a solution treatment at 800°C for 2 hours followed by water quenching. Subsequently, specimens were aged at 450°C for various lengths of time (3 to 16 hours) and water quenched. Samples which were not immediately examined were stored at -20°C to preclude aging at room temperature. Thinning for TEM examination was accomplished by a two stage process consisting of an initial jet polish to dimple the specimens, followed by final thinning to perforation by electropolishing. Details of the heat treatment and sample preparation techniques were developed previously by Mayes [Ref. 3]. The specimens were examined in a JEOL 100CX microscope operated at 120 kV, using a Gatan Model 636 double-tilt cooling holder to monitor and control the specimen temperature.

B. MATHEMATICAL PREDICTION EQUATIONS

The V-shaped contrast displays image extinctions similar to those ascribed to tweed contrast by Robertson and Wayman [Ref. 19] and others, indicating that static displacements within the matrix give rise to the observed V-shaped contrast. Accordingly, it was possible to determine the direction of shear displacements producing the images. In this analysis two possible static displacement directions were assumed:

$\mathbf{R} = \delta\{110\}/\langle 110\rangle$ and, $\mathbf{R} = \delta\{110\}/\langle 111\rangle$,

where δ is the atom displacement. The magnitude of atom displacement considered (from its perfect lattice position) is very small, corresponding to a small fraction of the interatomic distance. Figure 2.1 indicates these two possible displacement directions in a cubic crystal lattice.

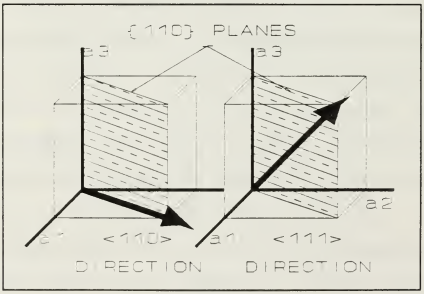

Figure 2.1 Cubic crystal illustrating one set of possible displacement directions.

Image contrast in the electron microscope is produced by electron diffraction. As such, electrons may be considered as particle waves with wavelength λ described by the de Broglie relation; $mv = h/\lambda$, where h is Planck's constant, m is the mass of an electron, and v is its velocity. At an accelerating voltage of 100 kV, which is typically used in electron microscopes, the relativistically corrected wavelength is 0.0037 nm. The very small wavelength of electron particle waves allows extremely high image resolution, approaching a value required to image the crystalline lattice directly. [Ref. 35]

In the transmission electron microscope (TEM), an electron beam is focussed on a thin specimen (typically 100-500 nm thick). The electrons interact with the specimen via elastic and inelastic scattering and emerge on the exit side of the specimen. Each individual atom within the specimen scatters the incident electron beam, however, the scattered wavelets interfere and will emerge in phase only in particular crystallographic directions. Bragg's law describes the relation which holds for electron diffraction within crystalline solids. For a strong (in phase) reflection, we must have;

$$2d_{(hkl)} \sin \theta = n\lambda, \quad \text{where}$$

$d_{(hkl)}$ is the interplanar spacing, θ is the angle of reflection, and $n\lambda$ is an integral number of wavelengths.

An objective lens focusses the emerging diffracted and transmitted beams to form a spot (diffraction) pattern in the back focal plane of the microscope. Images are produced on the viewing screen (or camera) by further focussing of this spot pattern.

Two important mechanisms produce image contrast in the TEM. **Diffraction contrast** arises by intercepting either the diffracted beams or the transmitted beam with an objective aperture. **Phase contrast** arises through the recombination of diffracted and transmitted beams at the exit surface of the specimen. The phase differences between the two beams which result are converted into intensity differences in the image.

Phase contrast is the dominant mechanism for object detail less than approximately 1 nm and is important in the study of early stages of short-range order. The two-beam dynamical theory of electron diffraction is a simplified approach to describe the resultant amplitudes of the emerging transmitted (ϕ_o) and diffracted (ϕ_g) beams. A pair of coupled, first order differential equations, known as the Darwin-Howie-Whelan equations, describe the interaction of the beams as they pass through the thickness z, of the thin foil:

$$\frac{d\phi_o}{dz} = \frac{i\pi}{\xi_o}\phi_o + \frac{i\pi}{\xi_g}\phi_g \exp(2\pi i s z)$$

$$\frac{d\phi_g}{dz} = \frac{i\pi}{\xi_g}\phi_g + \frac{i\pi}{\xi_o}\phi_o \exp(-2\pi i s z).$$

The additional terms in these equations are; **s**, the deviation from the exact Bragg angle, ξ_o and ξ_g, constants which describe a critical distance in the perfect crystal at which the intensity periodically falls to zero, known as the extinction distance.

A strict quantitative analysis of strain contrast requires the use of the dynamical theory of electron diffraction. However, in this case, where the extinction of images is due to static displacement, **R**, the use of kinematical theory is sufficient. For a locally distorted crystal, the distortion induces an extra phase factor exp(-iα), where $\alpha = 2\pi \mathbf{g}\cdot\mathbf{R}$, and where **g** is the reciprocal lattice vector of the operating diffracted beam in a two-beam condition. This phase factor can essentially be applied to the dynamical theory without change of the expression. The coupled differential equations describing the wave amplitudes become:

$$\frac{d\phi_o}{dz} = \frac{i\pi}{\xi_o}\phi_o + \frac{i\pi}{\xi_g}\phi_g \exp(2\pi i \mathbf{s} z + i\alpha)$$

$$\frac{d\phi_g}{dz} = \frac{i\pi}{\xi_g}\phi_g + \frac{i\pi}{\xi_o}\phi_o \exp(-2\pi i \mathbf{s} z - i\alpha).$$

The strain field contrast depends on the value of α, and image extinction occurs when α = 0. If we exclude the scaling factor (2π) and consider cartesian coordinates, $\mathbf{g}\cdot\mathbf{R}$ can be written as:

$$\mathbf{g}\cdot\mathbf{R} = g_x R_x + g_y R_y + g_z R_z.$$

Values of $\mathbf{g} \cdot \mathbf{R}$ other than 0 may be used to qualitatively indicate the strength of contrast in the directions determined, i.e., a value of 4 would produce a "stronger" image than say a value of 2. Thus, it is possible to determine the atomic displacement directions from the extinction rule, where $\alpha = 0$, and by assuming that images produced from line features in the crystal are projections on the film plane.

The mathematical relations which describe the directions of streaks in the diffraction patterns will be discussed in detail in a following section.

C. ANALYSIS OF FLICKER ENERGETICS

1. Equipment Description and Setup

The present research focused on the use of various data acquisition techniques to define specific characteristics of the flicker activity. This included the use of both video imaging and processing instruments to display image intensity in both time and frequency domains.

A spectrum analyzer coupled with a fiber optic image converter was used to "read" the time and frequency characteristics of the flicker sites directly from the TEM video imaging system TV screen. A video tape monitor was employed to record the dynamic images obtained during this analysis. Figure 2.2 illustrates the layout of the system.

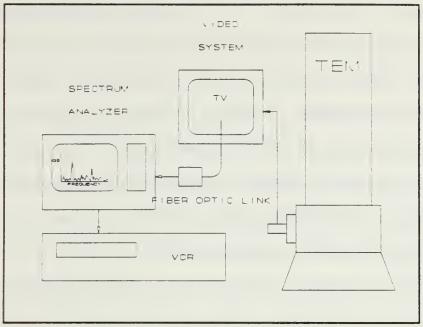

Figure 2.2 Experimental frequency monitoring setup.

System components used in this study included:

1. Transmission electron microscope: Specimens were examined in a JEOL 100CX TEM operated at 120 kv. Magnification at the TV monitor was approximately 300 kx.
2. Video imaging system: A Gatan Model 673 wide angle TEM-TV system was used; this employed a yttrium aluminum garnet (YAG) transmission scintillator directly linked to a charge coupled device via a fiber optic plate. Image resolution was better than 160 line pairs per cm at the YAG screen. The TV monitor was a SANYO model VM4509 (9 inch diagonal).

3. Image converter: A light sensitive photo transistor with a high gain preamp was coupled to the video screen via a fiber optic link. The output response in volts (0 to 1.2 V) was linearly proportional to the input image intensity, with a frequency response from 0 to 1 Megahertz. The details of construction of the image converter are presented in Appendix A.
4. Signal analyzer: A Scientific Atlanta Model SD380 spectral analyzer was used to process the signal input from the image converter. The frequency response of the analyzer was from 1 Hz to 40 kHz. The display setup used included both real time and averaged frequency (X scale) versus linear and log volts input (Y scale). Analyzer screen resolution (for spectrum displays) was 400 lines per screen. (400 lines on a 0 to 20 Hz window corresponded to 0.05 Hz per line resolution). Average frequency display used 500 counts (50.0 seconds) of real time data.
5. Specimen cooling stage: A Gatan Model 636 double tilt cooling holder with a temperature range of +80°C to -169°C (liquid Nitrogen temperature) was used to monitor and adjust specimen temperature.

2. Equipment Calibration

A calibration sequence was performed to determine the dynamic response of the frequency monitoring system. A blinking screen cursor, whose characteristics were independently verified, was displayed on the 9 inch TEM monitor screen to simulate a flicker site. (The cursor frequency and image area which this provided was approximately the same as a typical flicker site.) This image was "read" with the frequency analysis system and checked with data obtained from an oscilloscope. The frequency spectrum of the simulated flicker is plotted in Figure 2.3.

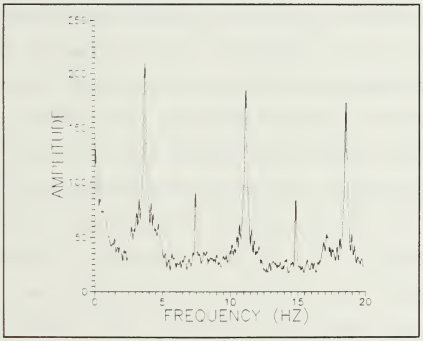

Figure 2.3 Calibration pulse frequency spectrum.

The first peak identifies the cycle time of the pulse (0.267 sec., corresponding to 3.75 Hz), the second smaller

peak equates to the "on" time of the pulse (0.133 sec. out of 0.267 sec; i.e., the pulse is on for half of the time.) Background noise is evident in the figure at a level of about 25 (corresponding to 0.5 mV). The background noise is a composite of the TEM image system scan, and (in some cases) tape recorder playback head scan.

Next, the time domain characteristics of the video screen raster were determined to ensure that an adequate window was available to capture the cycle time of a flicker site. The fiber optic probe light sensitive area (about 1 mm^2) read the intensity of a corresponding group of pixels on the TV screen. Since the pixels were illuminated only momentarily during the raster scan of the TV crt electron beam, any change in intensity must be sensed either during the pixel group illumination time, or over several scans of the pixel group. Figures 2.4 and 2.5 illustrate the character of the screen raster. The time difference between illuminations of a pixel group during a scan was 0.0167 seconds (corresponding to a 60 Hz fundamental frequency). The illumination rise time of a pixel group was 0.165 msec, illumination decay was 0.675 msec, with a total "on" time of 1.775 msec. This data sampling window proved adequate to define the relatively slow change in screen intensity of flicker motion.

A "standard" configuration of the monitoring system was established and used throughout the frequency

characterization sequence. Since the presence of video system scan (with a dominant 60 Hz fundamental) was superimposed on the frequency display, a window was chosen to exclude this frequency. In order to standardize the output, a window from 0 to 20 Hz was used for all plots, this being the frequency range estimated by visual means. (Higher frequencies were occasionally checked to ensure that this window was adequate.) The 0 to 20 Hz window used, with 400 frequency bins, provided a resolution of 0.05 Hz, which was considered adequate for the frequency plots.

The vertical scale (Y-scale) for frequency spectra was selected to conform to the output characteristics of the fiber optic image converter (0 to 1.2 volts).

In addition to the real time display of frequency spectra an average (AVG) capability was used. In this display the real time data is averaged over a selectable interval (50.0 seconds used here). This provides better identification of dominant frequencies over background noise.

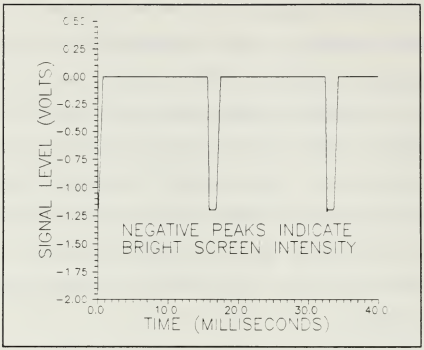

Figure 2.4 Video scan time history plot showing cycle time of screen raster.

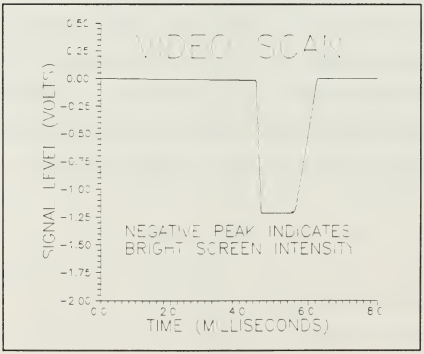

Figure 2.5 Video scan time history plot. Enlargement of pixel illumination time period.

III. RESULTS AND DISCUSSION

A. DETERMINATION OF SHEAR DISPLACEMENTS

1. Image Extinction Analysis

Detailed analysis of the tweed contrast in numerous systems, such as aged Fe-Pd alloys [Ref. 33], and aged Cu-Zn alloys [Ref. 34], has revealed that the lines of contrast (the tweed "striations") typically lie along traces of {110} planes of a cubic phase, and obey extinction rules which are consistent with them being due to underlying net <110> shear distortions of {110} planes.

In the present case of well-aged Cu-Mn alloys, the tweed contrast has largely been supplanted by a V-shaped localized contrast, but the dominant image axis of the V-shaped morphology also lies along traces of {110} planes, i.e., along the same traces which (at shorter aging times) were defined by the tweed striations. This is clear in the static photograph taken from the (100) image plane which is presented in Figure 3.1. The V-shapes often appear in parallel clusters, with adjacent V's pointing in opposite directions, forming a sort of zigzag pattern. In this case, the zigzag image contrast resembles a miniaturized group of self-accommodating crystal units, a morphology which is well-known in thermoelastic martensites. The use of stereographic microphotography was attempted to resolve the spatial

orientation of the V-shaped images in the thickness direction of the foil, and will be discussed in detail later on.

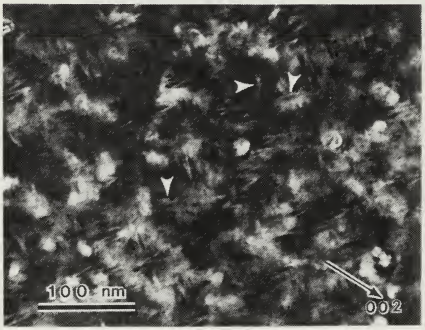

Figure 3.1 Alloy aged 10 hours at 450°C. Static exposure of (100) image plane illustrating V-shaped images lying parallel to traces of (110) planes. Two beam bright field image with $\mathbf{g}$ = 002.

Image extinctions for three low-index crystallographic zones; (100), (110), and (111), were predicted for both displacement directions, <110> and <111>. The predicted image extinctions were then compared with those actually observed in images from a Cu-Mn-Al alloy aged for 10 hours at 450°C which displayed the V-shaped and zigzag morphologies. In each case a "truth table" of dot products was calculated for $\mathbf{g}\cdot\mathbf{R}$, and this product used to predict the expected image axis directions and qualitative contrast intensities.

Tables 3.1 through 3.6 and Figures 3.2 through 3.13 present the values of $\mathbf{g}\cdot\mathbf{R}$ and image predictions for these projections and compare them with what has been observed. A "boxed" axis arrangement, with V's superimposed, is used to aid in illustrating the image predictions.

TABLE 3.1 DOT PRODUCT VALUES OF $\mathbf{g}\cdot\mathbf{R}$.
(100) ZONE, **R** OF THE FORM <110>.

Direction **R**	**g**: 0-2 2	**g**: 0 0 2	**g**: 0 2 2	**g**: 0 2 0
δ [1 1 0]	-2	0	2	2
δ [1 0 1]	2	2	2	0
δ [0 1 1]	0	2	4	2
δ [1-1 0]	2	0	-2	-2
δ [1 0-1]	-2	-2	-2	0
δ [0-1 1]	4	2	0	-2

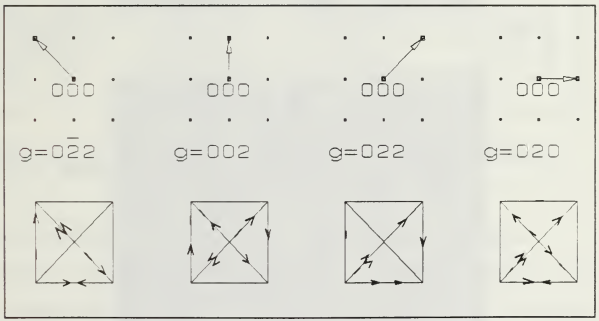

Figure 3.2 Predicted images on (100) plane for **g** vectors shown. **R** of the form <110>. Images appear parallel to <001> and <110> directions.

TABLE 3.2 DOT PRODUCT VALUES OF **g**·**R**.
(100) ZONE, **R** OF THE FORM <111>.

Direction **R**	**g**: 0-2 2	**g**: 0 0 2	**g**: 0 2 2	**g**: 0 2 0
δ [1 1 1]	0	2	4	2
δ [1-1 1]	4	2	0	-2
δ [-1-1 1]	4	2	0	-2
δ [-1 1 1]	0	2	4	2

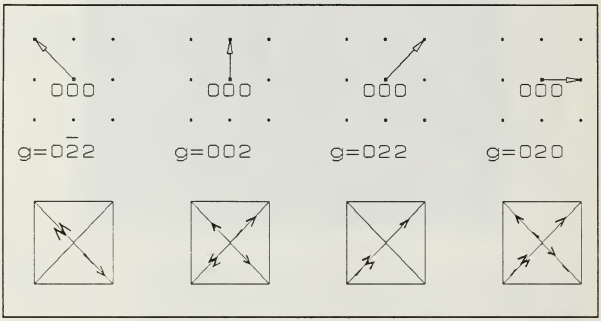

Figure 3.3 Predicted images on (100) plane for **g** vectors shown. **R** of the form <111>. Images appear only in <011> directions.

The actual TEM images, oriented with the <110> zone axis parallel to the incident election beam are shown in Figures 3.4 and 3.5. Since the images for **g** = 0-2 2 and 0 2 2 are identical relative to the initial axis orientation, only one photograph is required using either of these diffracting vectors to identify the V-image directions. The same applies for **g** = 0 0 2 and 0 2 0. The actual images more closely match

those predicted for a shear displacement direction R of the form <111>.

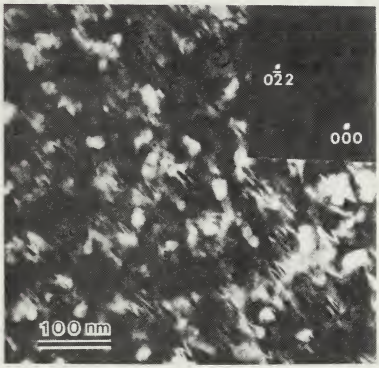

Figure 3.4 (100) zone. Two-beam bright field image obtained with g = 0-2 2.

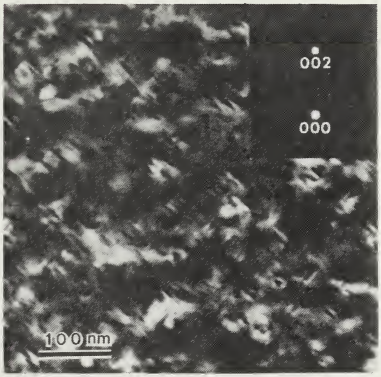

Figure 3.5 (100) zone. Two-beam bright field image with g = 0 0 2.

TABLE 3.3 DOT PRODUCT VALUES OF **g**·**R**.
(110) ZONE, **R** OF THE FORM <110>.

Direction **R**	**g**: -1 1 1	**g**: 0 0 2	**g**: 1-1 1	**g**: 2-2 0
δ [1 1 0]	0	0	0	0
δ [1 0 1]	0	2	2	2
δ [0 1 1]	2	2	0	-2
δ [1-1 0]	-2	0	2	4
δ [1 0-1]	-2	-2	0	2
δ [0-1 1]	0	2	2	2

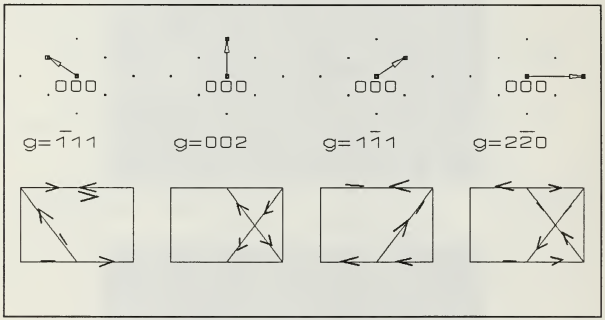

Figure 3.6 Predicted images on (110) plane for **g** vectors shown. **R** of the form <110>. The images should appear along traces parallel to <112> and <110> directions.

TABLE 3.4 DOT PRODUCT VALUES OF **g**·**R**.
(110) ZONE, **R** OF THE FORM <111>.

Direction **R**	**g**: -1 1 1	**g**: 0 0 2	**g**: 1-1 1	**g**: 2-2 0
δ [1 1 1]	1	2	1	0
δ [1-1 1]	-1	2	3	4
δ [-1-1 1]	1	2	1	0
δ [-1 1 1]	3	2	-1	-4

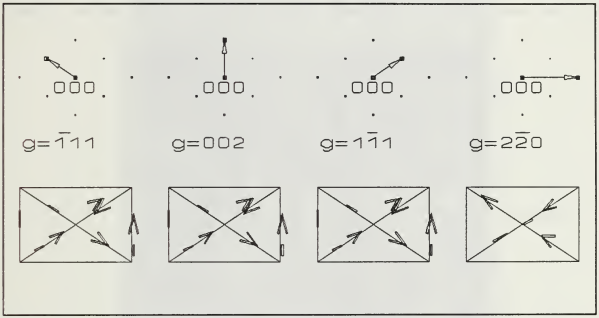

Figure 3.7 Predicted images on (110) plane for **g** vectors shown. **R** of the form <111>. The images should appear along traces parallel to <110> and <001> directions.

Figures 3.8 through 3.10 present the TEM images with the <110> zone axis parallel to the incident electron beam. As with the analysis for the <100> zone axis, two of the diffracting vector orientations are redundant, and only one such photograph taken with either **g** = -1 1 1 or 1-1 1 was required. The comparison of actual and predicted images is not as straightforward as in the previous (<100> zone axis)

case. For example, the included minor angle between V-image axis directions does not precisely "fit" either prediction. The qualitative "strength" of image for a given diffracting vector must be applied to gage which prediction more closely matches actual images. If this is done, the predictions with **R** of the form <111> better match actual TEM images. A detailed comparison is presented later for all image zones.

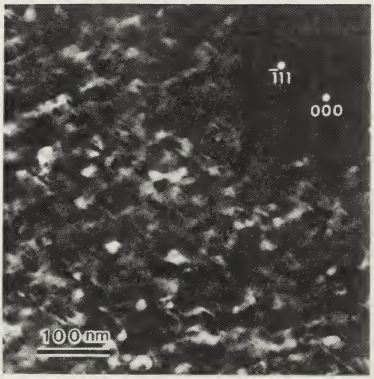

Figure 3.8 (110) zone. Two-beam bright field image obtained with **g** = -1 1 1.

Figure 3.9 (110) zone. Two-beam bright field image obtained with **g** = 0 0 2.

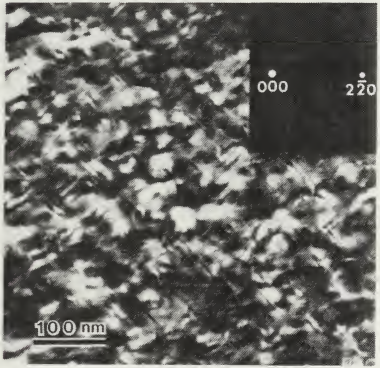

Figure 3.10 (110) zone. Two-beam bright field image obtained with **g** = 2-2 0.

TABLE 3.5 DOT PRODUCT VALUES OF **g**·**R**.
(111) ZONE, **R** OF THE FORM <110>.

Direction **R**	**g**: -2 2 0	**g**: -2 0 2	**g**: 0-2 2
δ [1 1 0]	0	-2	-2
δ [1 0 1]	-2	0	2
δ [0 1 1]	2	2	0
δ [1-1 0]	-4	-2	2
δ [1 0-1]	-2	-4	-2
δ [0-1 1]	-2	2	4

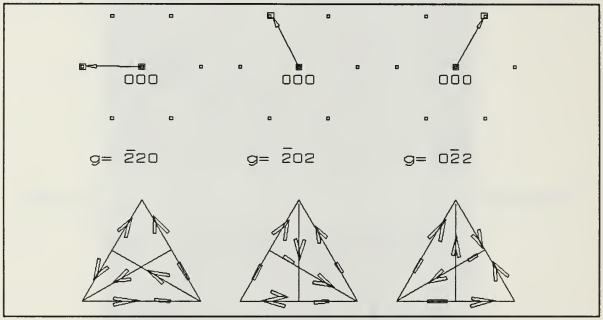

Figure 3.11 Predicted images on (111) plane for **g** vectors shown. **R** of the form <110>. The images should appear along traces parallel to <1-1 0> and <-1-1 2> directions.

TABLE 3.6 DOT PRODUCT VALUES OF $\mathbf{g}\cdot\mathbf{R}$.
(111) ZONE, **R** OF THE FORM <111>.

Direction **R**	**g**: 2 2 0	**g**: 2 0 2	**g**: 0 2 2
δ [1 1 1]	0	0	0
δ [1-1 1]	-4	0	4
δ [-1-1 1]	0	4	4
δ [-1 1 1]	-4	4	0

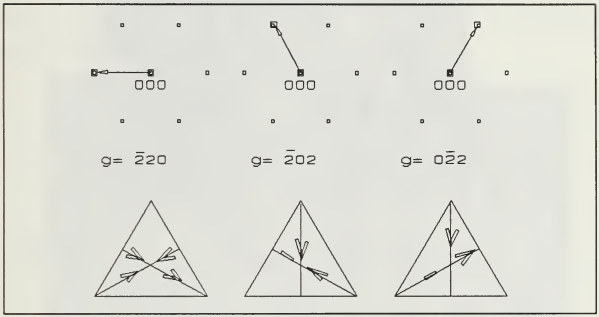

Figure 3.12 Predicted images on (111) plane for **g** vectors shown. **R** of the form <111>. The images should appear along traces parallel to <-1-1 2> direction.

Figure 3.13 presents an actual TEM image with the <111> zone axis parallel to the electron beam. Only one photograph is required for this image plane since the **g** vectors used are redundant. The actual images more closely match those predicted for a shear displacement direction of the form <111>.

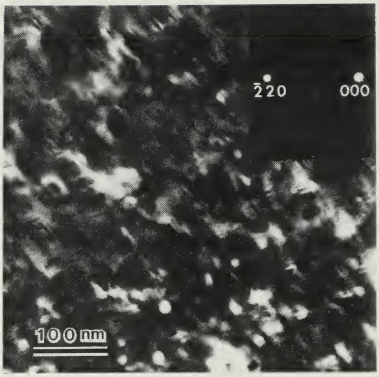

Figure 3.13 (111) zone. Two-beam bright field image obtained with g = -2 2 0.

2. Diffraction Spot Streak Analysis

As well as the development of the V-shaped contrast during aging, streaks appear on spots in selected area diffraction patterns. The streaks are diffuse and lie along specific directions. Figure 3.14 illustrates an enlargement of a (100) zone diffraction pattern of a specimen aged for 10 hours at 450°C, showing the streaks present at the transmitted and diffracted spots.

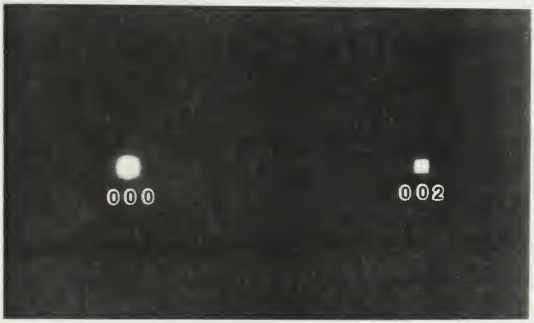

Figure 3.14 Selected area diffraction pattern of alloy aged 10 hours at 450°C. (100) zone. Both transmitted, 000, and diffracted, 002 spots are shown enlarged.

The presence of the streaks in the diffraction patterns can also be used to characterize the microstructure of the area selected for imaging. Streaking of diffraction spots can originate from either the shape of crystal defects or from lattice strain associated with them. (The term

streaking is synonymous with the broadening, elongation, or splitting of reciprocal lattice points.) Because shape and strain effects can occur simultaneously and have similar appearance, it is often difficult to distinguish streaking produced by lattice strain from that produced by shape effects of particles. [Ref. 35] Both mechanisms are discussed in greater detail below, along with their key distinctions.

a. Shape Effects

The geometry of lattice imperfections or precipitates can cause streaking of diffraction spots. For precipitates of a particular shape, the intensity distribution at a reciprocal lattice point is increased in directions perpendicular to the thin dimensions of the particle. Thus the shape of a precipitate particle during the early stages of development may be deduced from analysis of the streaks in the SADP. It should be realized that if the particles are small, (as expected in the early stages of aging), they might not contribute to the image directly by diffraction. Thus, the only indication of the presence of very small precipitates of a particular shape is via diffraction spot streaking.

A key identifying feature of streaking resulting from shape effects is that the broadening occurs equally over the field of the diffraction pattern, including the 000 transmitted spot. Additionally, the streaks will maintain their presence and alignment regardless of the direction of the diffracting vector. A schematic representation of

streaking produced from thin platelets within the foil is displayed in Figure 3.15 [Ref. 35].

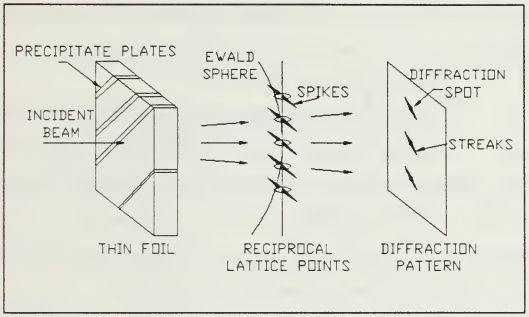

Figure 3.15 Streaking of reciprocal lattice points developed from shape effect of precipitates. (Adapted from Edington, Ref. 35)

An estimate of the thickness of the platelets can be made based on the amplitude distribution in reciprocal space. For spherical precipitates, the intensity distribution would be spherically symmetrical; for plate-like precipitates, the intensity distribution would be in the form of a spike normal to the plate; and for needle shaped precipitates, the intensity distribution would take the form of a disk in reciprocal space. Thus, in general, the intensity distribution will be extended along directions parallel to the shortest dimension of the precipitate. In the present case, as the specimen is tilted, the range of sample

orientation, $d\phi$, over which the streak intensity is appreciable, is observed to be quite large. This range of sample orientation, $d\phi$, is inversely proportional to the platelet thickness, t. A large value of $d\phi$ indicates very thin platelets (of the order of 10's of nm). [Ref. 36]

b. Elastic Strain Effects

Elastic strain produced from coherent precipitates within a crystal matrix can also cause streaking of diffraction spots. The reciprocal lattice spikes produced in this way will be aligned with the direction of lattice distortion. The main characteristics associated with elastic strain effects can be summarized as follows:

1. The magnitude of elongation of the diffraction spot is a function of the distance from the transmitted 000 spot. Streaks appear broader as the indices of the reciprocal lattice point increase. Additionally, the streaks associated with a given diffraction spot will generally appear on the side toward the transmitted spot.
2. No streaks occur at the transmitted spot itself.
3. No streaks appear along distortion directions that lie in the reflecting plane. (Streaks due to lattice distortion from elastic strain obey the extinction rules described earlier.)

Figure 3.16 presents a schematic representation of streaking produced by strain field effects along <110> crystal directions [Ref. 35].

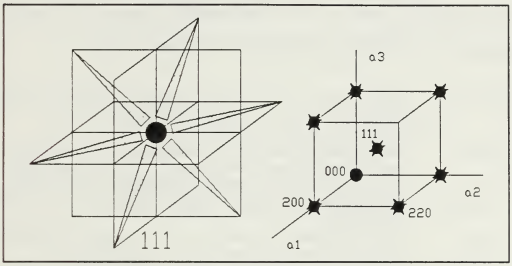

Figure 3.16 Streaking of reciprocal lattice points developed from elastic strain field effects. Enlargement of the 111 reciprocal lattice point with streaks missing in distortion directions lying in reflecting plane. (Adapted from Edington, Ref. 35)

In the present Cu-Mn-Al samples, aged to display V-shaped image contrast, diffraction spot streaking is a subtle effect and is believed to be caused predominantly by the presence of thin disk or platelet shaped regions. The orientation of the thin dimension of the platelets is normal to the direction of the spikes in reciprocal space.

c. Prediction and Analysis

The streaks present in the diffraction patterns can be used to systematically define the habit planes of the platelets producing the streaking. In this analysis the

intersection between the Ewald sphere of reflection and the reciprocal lattice spike is considered to determine the position of the corresponding diffraction spot. It is convenient to define the following terms to aid in the mathematical analysis (refer to Figure 3.17):

[uvw]	-	Zone axis of electron beam passing through crystal. (Also defines the crystal orientation in view.)
[pqr]	-	Reciprocal lattice direction of spikes. (Also defines the direction of lattice distortion for strain effects, and the direction of the thin dimension for shape effects.)
hkl	-	Coordinates of point P in (uvw) reciprocal lattice plane.
[p'q'r']		Direction of streaking produced by the [pqr] reciprocal lattice spike projected on the image plane.
(u'v'w')		Reciprocal lattice plane.

The direction [p'q'r'] of the streak can be predicted assuming a given orientation of platelet for a particular zone axis [uvw] by the following relation for cubic crystals:

$$[p'q'r'] = [p(v^2+w^2)-u(rw+qv);\ q(u^2+w^2)-v(pu+rw);\ r(u^2+v^2)-w(pu+qv)].$$

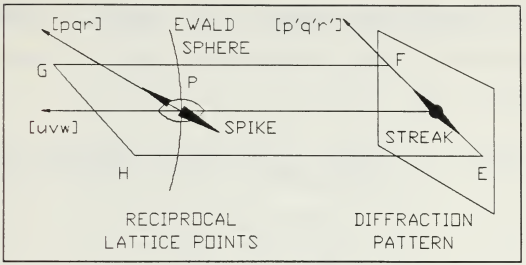

Figure 3.17 Direction of streaking ([p'q'r']) produced by a [pqr] reciprocal lattice spike.

Selected area diffraction patterns (SADP) taken at near-perfect Bragg conditions in the (100) zone show subtle but definite streaking along <011> directions. Such streaks could result from spike directions of <111> or <110>. Therefore predictions of diffraction pattern streaks were made for these two spike directions. The resultant predictions are a superposition of all calculated streak directions. The consideration of streak extinctions when $\mathbf{g}\cdot\mathbf{R}=0$ has been excluded, since we postulate that the streaking is predominantly due to shape effects.

The [p'q'r'] streak direction predictions are tabulated in Tables 3.7 through 3.12 for each [p q r] reciprocal lattice spike direction, and [u v w] zone axis combination. Predicted diffraction patterns and streak directions are presented following each data table, along with

actual diffraction patterns for comparison (including enlargements of the transmitted 000 spot) in Figures 3.18 through 3.27.

TABLE 3.7 DIFFRACTION SPOT STREAK DIRECTIONS FOR (100) CRYSTAL PLANE, [pqr] OF THE FORM <110>.

[p q r]	[u v w]	[p'q'r']
[1 1 0]	[1 0 0]	[0 1 0]
[1 0 1]	[1 0 0]	[0 0 1]
[0 1 1]	[1 0 0]	[0 1 1]
[1-1 0]	[1 0 0]	[0-1 0]
[1 0-1]	[1 0 0]	[0 0-1]
[0-1 1]	[1 0 0]	[0-1 1]

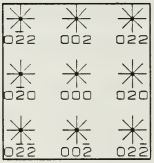

Figure 3.18 Predicted streak directions on (100) image plane for <110> spike directions.

TABLE 3.8 DIFFRACTION SPOT STREAK DIRECTIONS FOR (100) CRYSTAL PLANE, [pqr] OF THE FORM <111>.

[p q r]	[u v w]	[p'q'r']
[1 1 1]	[1 0 0]	[0 1 1]
[-1 1 1]	[1 0 0]	[0 0 0]
[1-1 1]	[1 0 0]	[0-1 1]
[-1-1 1]	[1 0 0]	[0-1 1]

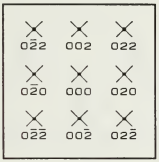

Figure 3.19 Predicted streak directions on (100) image plane for <111> spike directions.

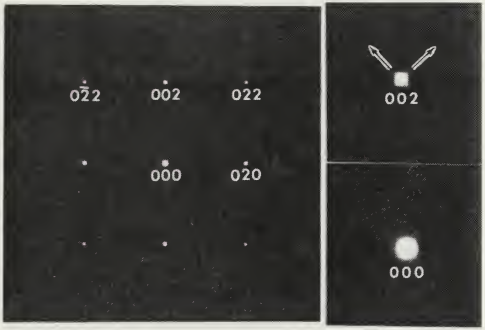

Figure 3.20 Selected area diffraction pattern of (100) image plane showing streaking along <110> directions. Enlargement of transmitted 000 spot and 002 spot included.

TABLE 3.9 DIFFRACTION SPOT STREAK DIRECTIONS FOR (110) CRYSTAL PLANE, [pqr] OF THE FORM <110>.

[p q r]	[u v w]	[p'q'r']
[1 1 0]	[1 1 0]	[0 0 0]
[1 0 1]	[1 1 0]	[1-1 2]
[0 1 1]	[1 1 0]	[-1 1 2]
[1-1 0]	[1 1 0]	[2-2 0]
[1 0-1]	[1 1 0]	[1-1-2]
[0-1 1]	[1 1 0]	[1-1 2]

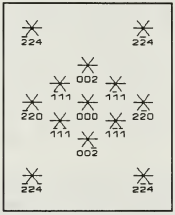

Figure 3.21 Predicted streak directions on (110) image plane for <110> spike directions.

TABLE 3.10 DIFFRACTION SPOT STREAK DIRECTIONS FOR (110) CRYSTAL PLANE, [pqr] OF THE FORM <111>.

[p q r]	[u v w]	[p'q'r']
[1 1 1]	[1 1 0]	[0 0 1]
[-1 1 1]	[1 1 0]	[-1 1 1]
[1-1 1]	[1 1 0]	[1-1 1]
[-1-1 1]	[1 1 0]	[0 0 1]

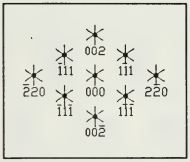

Figure 3.22 Predicted streak directions on (110) image plane for <111> spike directions.

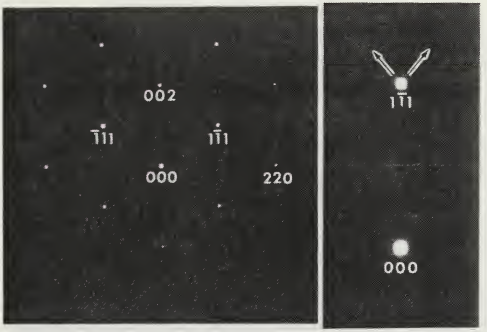

Figure 3.23 Selected area diffraction pattern of (110) image plane showing streaking along near <111> directions. Enlargement of transmitted 000 spot and 1-1 1 spot included.

TABLE 3.11 DIFFRACTION SPOT STREAK DIRECTIONS FOR (111) CRYSTAL PLANE, [pqr] OF THE FORM <110>.

[p q r]	[u v w]	[p'q'r']
[1 1 0]	[1 1 1]	[1 1-2]
[1 0 1]	[1 1 1]	[1-2 1]
[0 1 1]	[1 1 1]	[-2 1 1]
[1-1 0]	[1 1 1]	[1-1 0]
[1 0-1]	[1 1 1]	[1 0-1]
[0-1 1]	[1 1 1]	[0-1 1]

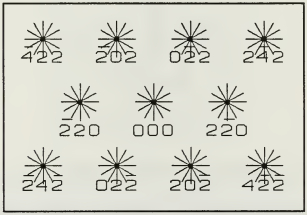

Figure 3.24 Predicted streak directions on (111) image plane for <110> spike directions.

TABLE 3.12 DIFFRACTION SPOT STREAK DIRECTIONS FOR (111) CRYSTAL PLANE, [pqr] OF THE FORM <111>.

[p q r]	[u v w]	[p'q'r']
[1 1 1]	[1 1 1]	[0 0 0]
[-1 1 1]	[1 1 1]	[-4 2 2]
[1-1 1]	[1 1 1]	[2-4 2]
[-1-1 1]	[1 1 1]	[-2-2 4]

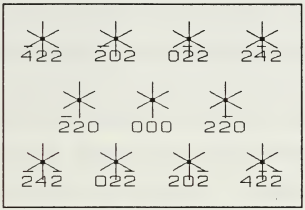

Figure 3.25 Predicted streak directions on (111) image plane for <111> spike directions.

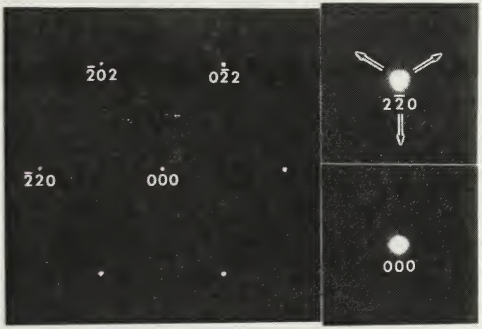

Figure 3.26 Selected area diffraction pattern of (111) image plane showing streaking along <121> directions. Enlargement of transmitted 000 spot and 2-2 0 spot included.

3. Analysis of Streaks at the Transmitted Spot

The presence of streaking at the transmitted 000 spot of the diffraction pattern is a key indicator of the presence of thin platelets within the matrix of the parent phase. It should be noted that the elastic strain effect of broadening of the reciprocal lattice points in the SADP is masked by the shape effect described earlier. Thus, if any strain of the matrix is present, this method of analysis cannot distinguish it.

It should be noted that samples aged for short times (which display tweed) show no evidence of streaks at the 000 spot, indicating that the incipient transformation of the platelets has not yet occurred, or is below the threshold of detection.

4. Stereoscopic Examination of V-Shaped Contrast

An attempt at stereoscopic observation of the V-shapes was made in order to ascertain their three-dimensional distribution and orientation, similar to experiments performed by Oshima, et al., on the tweed contrast of Fe-Pd alloys [Ref 33]. Dual dark field (DF) images were made (using high order diffraction spots i.e., 008, 00-8 and 0010, 00-10 pairs) by tilting the specimen while observing the same area. The high order reflections produced the "tilt" of approximately 5 degrees needed for a reasonable stereoscopic effect.

The stereoscopic observations of Oshima [Ref. 33] showed that Fe-Pd tweed was displayed as separated spherical

or stick-like strain field contrasts with densities apparently larger in the vicinity of both surfaces than within the interior of the specimen. However, the conclusion that the actual structure underlying the tweed has a spatial arrangement similar to that of the observed contrast density cannot be made, since this very effect is predicted by the dynamical theory of image contrast. For thin specimens, the dynamical theory predicts greater image contrast for features lying close to the foil surfaces than for features near the foil centerline. In other words, an apparent spatial variation in contrast may be seen even though the features producing the contrast are evenly dispersed within the thickness of the foil, and a false indication of feature density and distribution may result.

Figure 3.27 presents a stereographic pair of V-shaped images near a point of spatial reference (dual holes near the lower center of the image field). Appendix B discusses viewing of stereographic pairs without the aid of a viewer.

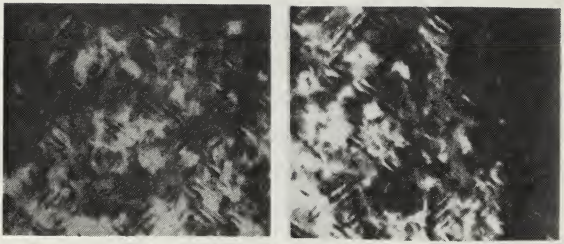

Figure 3.27 Stereographic image pair of V-shaped image.

Experimental results in the present case indicate no distinct angular orientation of the V-images with respect to the specimen normal. The stereo "3-D effect" produced is distorted by the dynamic nature of the V-shaped flicker sites, with the image contrast changing with time as well as with the angle of the beam axis. Additionally, errors in image projection arise from displacement differences in the projected positions of the V sites.

5. Summary of Experimental Observations

The following paragraphs summarize the observations made from the image extinction and diffraction pattern streak analysis.

The image axes of the V-shaped images lie along traces of {110} planes. (This corresponds to <022> directions on the

image plane.) This is most evident in the <100> normal image plane. These images (for the <100> normal image plane) precisely fit the predictions for a displacement or distortion of the form <111> on {110} planes, with no discrepancies. On the other hand, image predictions for a matrix distortion of the form <110> include an additional contrast trace direction of <100>, but these images are not present. The $\mathbf{g}\cdot\mathbf{R}$ dot product value of these invisible images is of lower value than for the predicted trace directions which actually appear; i.e., a value of 4 for the <110> axis direction (visible) as compared with a value of 2 for the <100> axis direction (invisible). Thus it is possible that this "lower order" image trace direction (<100>) is simply too diffuse to be visible, in which case, matrix distortion of the form <111> "fits" the extinction analysis for this image plane.

For certain operating g-vectors, the V-shapes observed on the <110> normal image plane do not exactly fit the predictions for either <111> or <110> displacements. The traces observed on this image plane lie in projected <111> directions. The minor angle between image axes varies between 68° and 82°, centered along the <220> direction, where an angle of 70° corresponds to the subtended minor angle between (111) planes or <111> directions.

Even if we consider that the V-shaped contrast exists only near the foil surfaces, i.e., a "surface effect", the observed images still lie along traces of {110} planes,

similar to the classic definition of tweed contrast. The intersections of these {110} planes with the <110> normal image plane produce traces which lie along <111> directions.

Several of the predicted images do not appear in the (110) zone for assumed displacements of either <111> or <110>. For example, when we assume matrix displacements of the form <110>, images which should lie along <220> directions are not present. For the **g**-vectors -1 1 1 and 0 0 2, the calculated dot product value is 2 for these (invisible) images. However, the dot product value is the same as for the images lying along <112> directions, which do appear. Also, for **g** = 2-2 0, the dominant image axis should be in the <220> direction, with a dot product value of 4; no such image is present. The predicted subtended minor angle between <112> image axes is 72° 32' centered along the <002> direction.

If the matrix displacement is assumed to be of the form <111>, images which should lie along <002> directions are not present. For **g**-vector -1 1 1 or 1-1 1, the calculated dot product value is 1 for traces along the <002> direction, and is the same for the <110> axis direction which is near perpendicular to **g**, where we expect extinction to occur. Thus we might conclude that a dot product value of 1 is too weak to produce the expected images. Traces only appear near <110> directions which are parallel to **g**, with a resulting dot product value of 3. For **g**-vector 0 0 2, all dot product values equal 2. Only traces which lie near the <110>

directions appear and predicted traces parallel to **g** do not appear. The predicted subtended minor angle between <111> image axes is 72° 32' but centered along the <220> direction.

Based on the observed minor subtended angle of approximately 70°, centered along the <220> direction, and the values of dot product of the predicted traces (which do not appear) being equal to the value of those traces expected to be extinct (near perpendicular to **g**), a "better fit" is achieved for matrix displacements of the form <111>.

Images observed on the <111> normal image plane exactly fit the predictions for matrix distortions of the form <111>. Images appear parallel to <112> directions. The subtended minor angle between V-shaped image axes is about 60 degrees.

On the other hand, if the matrix displacement is of the form <110>, images which are predicted to lie along <110> directions are not present. The dot product value of certain <110> predictions which are parallel to the operating **g** vector are large (value equals 4), compared to the images which are present (value equals 2). Thus, the dominant image axis should be expected to be parallel to **g**, but such traces are not present. Predicted subtended minor angles between expected image axes are 30° and 60°.

Streaking is present only in the diffraction patterns of samples aged for relatively longer aging times corresponding to the appearance of the V-shaped contrast. No

streaking is evident in samples aged at shorter times, which display well-developed tweed contrast. This observation differs from that of Oshima, et al. [Ref. 33], who reported that tweed in Fe-Pd alloys does show streaking in the SADP. In that case, the streaks observed obeyed the extinction rules for $\mathbf{g}\cdot\mathbf{R} = 0$, and streaks were observed at the 000 central spot.

Streaks in the present samples are observed at the 000 transmitted spot, and are not affected by the operating g vector which is selected. The streaks present at the transmitted spot, and the absence of streak extinction for g-vectors perpendicular to the streaks, are key indicators of shape effects due to defects or precipitates. Streaks due to elastic strain effects may indeed be present, but are masked by the predominance of the shape effect. (Streaks due strictly to elastic strain would obey the extinction rule of $\mathbf{g}\cdot\mathbf{R} = 0$, where R is the direction of matrix distortion.)

In the (100) image plane, streaks lie only along <110> directions, and the included angle between streaks is 90°. These streaks precisely fit the predicted streak directions on the (100) image plane for reciprocal lattice spikes in <111> directions, which correspond to platelet normals of <111>.

On the other hand, predicted streak directions for <110> reciprocal lattice spikes include <100> streak directions. These are not present. The included angle for

such streaks would be 45°. The streaking present in diffraction patterns of the (100) plane of Cu-Be alloys studied by Tanner (1966) [Ref. 18] show both <110> and <100> streak directions.

Streaks observed in the (110) image plane display a minor included angle of approximately 82°, centered along the <100> direction. This does not fit either assumed spike direction. Six streaks are predicted (vice the 4 observed) for either assumed spike direction. The predicted minor included angles for each assumed spike direction are: for <110>, 54° 44' and 73° 13', centered along <100>; for <111>, 73° 13' and 54° 44', centered along <110>. The actual observed streak directions correspond approximately to <210> or <310> directions.

B. ENERGETICS OF FLICKER ACTIVITY

1. General Nature of Flicker Activity

A sample of Cu-Mn-Al alloy (aged at 450°C for 10 hours) which displayed significant flicker activity was examined over a temperature range of -169°C to +80°C with various beam current settings. This heat treatment also corresponded to a peak in specific damping capacity for the alloy [Ref. 37]. Dark field examination with a <100> foil normal orientation produced the optimum change in contrast (bright to dark) during a flicker event, and was chosen throughout the present analysis to provide the highest signal-to-noise ratio for the optical probe. A typical field of view on the TEM video screen, including the optical probe area, and locations of typical flicker sites, is shown in Figure 3.28.

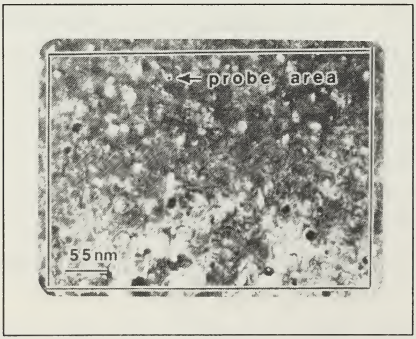

Figure 3.28 TEM display of flicker sites available on video screen. Probe sensing area shown for comparison.

It is important to note that the flicker activity was spatially dependent, varying considerably with location over the span of the field of view.

Figure 3.30 illustrates a selected time history record of a typical flicker sight, and displays the characteristics of a random signal. The (negative) peaks correspond to events of bright contrast at the flicker site, with the amplitude proportional to the intensity produced on the video screen. The jagged appearance of the time history results from the small sample window discussed earlier. If the time scale is reduced, a gradual change in contrast can be detected. ("Gradual" means occurring over several pixel illumination periods of 0.0167 seconds each.) When the time scale is expanded, as in Figure 3.31, an individual flicker event is revealed as undergoing a gradual change in intensity, which implies a gradual transition of the underlying crystal.

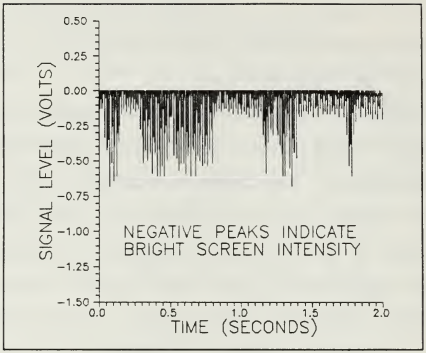

Figure 3.30 Time history record of a typical flicker site.

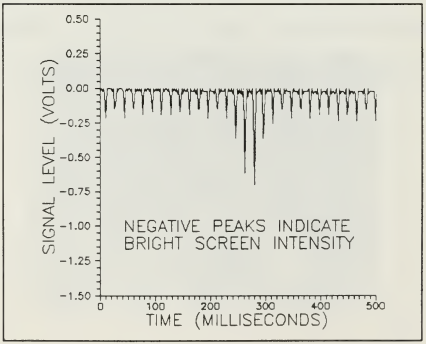

Figure 3.31 Expanded time history plot of a selected flicker site showing gradual intensity change.

In addition to the time histories of individual flicker sites, the frequency spectra of the intensity variations were recorded. With this technique it was possible to monitor the transitional characteristics of the small sections of the crystal lattice as various control parameters were altered. The spectrum obtained from a given field of view typically displayed a broadband of frequencies, with no distinct peaks. Time averaged frequency displays were used to reduce the amplitude variation and display periodic frequencies better than from the real time data stream. Although time averaged data tended to mask the underlying singular events, it was useful to illustrate general trends in the transitional behavior of the microstructure.

A surprising effect noted during this analysis was that some areas of flicker activity displayed "resonant" peaks or spikes in the frequency spectrum, indicating that periodicity exists in the variation of contrast intensity, and so in the crystallographic reorientation. The presence of multiple peaks at various frequencies indicated that several modes of oscillation occurred simultaneously. The frequency spectra are discussed in the next sections.

2. Variations in Activity with Specimen Temperature

The occurrence of resonant peaks in the frequency spectrum was dependant upon the specific site selected in the field of view, the temperature of the specimen, and the beam current setting of the TEM. The number of flicker sites which

displayed the phenomenon of resonance was very limited. It was estimated that less than 5 percent of the sites which were examined showed this effect. In order to investigate the peaks in the frequency spectrum further, specimen temperature was varied while maintaining a constant beam current.

Quantitatively, the number of flicker sites present was a function of specimen temperature. Low temperatures yielded few sites which displayed motion in samples with this aging treatment. As temperature was raised, the number of sites in the field of view increased. As temperature was varied, certain regions became active, while the motion in other regions diminished. No correlation could be obtained as to the rate of motion with temperature.

The behavior of several harmonic peaks (at approximately 5.0, 9.0, 12.7, 15.4, and 19.1 Hz) as temperature was raised (from -179°C to + 80°C) is shown in Figures 3.32 through 3.34. The peaks at these frequencies increased to a maximum near room temperature, then decreased as temperature was raised further. The appearance of harmonics in a frequency spectrum as certain control parameters are varied is an indicator of chaotic behavior, as will be discussed later on.

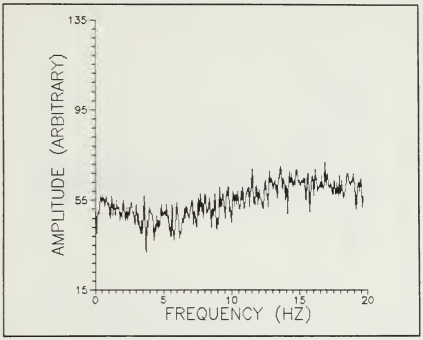

Figure 3.32 Frequency spectrum of selected flicker site. Specimen temperature -50°C.

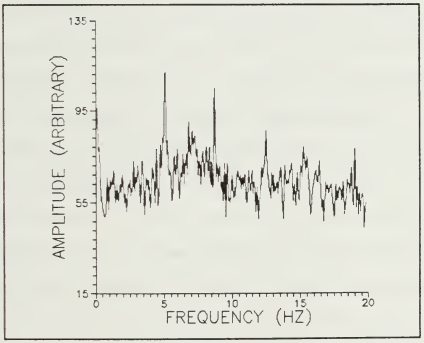

Figure 3.33 Frequency spectrum of selected flicker site. Specimen temperature +17°C.

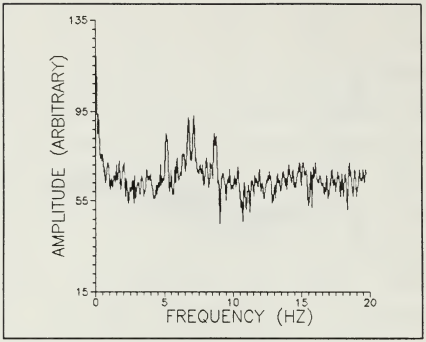

Figure 3.34 Frequency spectrum of selected flicker site. Specimen temperature +66°C.

3. Activity Correlation with TEM Beam Current

The effect on flicker activity of varying beam current while holding the specimen temperature constant was also examined. Specimen temperature was monitored and maintained using the cooling-heating stage. Certain resonance frequencies were discovered to be common to a variety of locations over the field of view. Checks were made to ascertain that this phenomenon was not a manifestation of the scintillation element in the TEM camera; the resonance was always associated with a flicker site, never with a static image; the characteristic low amplitude noise spectrum of a "pure" beam is shown in Figure 3.35.

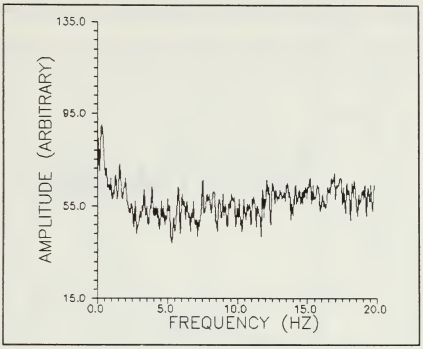

Figure 3.35 Frequency scan of e-beam on TEM video image system camera. Beam current 100 μA.

The nature of resonant peaks at a flicker site is represented by the spectrum shown in Figure 3.36, taken from a sample aged at 450°C for 10 hrs when examined in a <100> foil normal orientation with beam current held at 100 μA. Strong peaks are seen in this case at 3.60, 5.25, 8.85, 10.45, 14.50, 17.65, and 19.30 Hz.

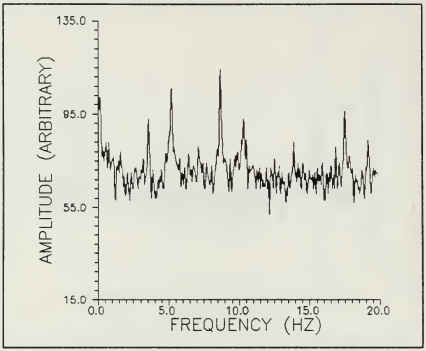

Figure 3.36 Frequency spectrum of sample aged at 450°C for 10 hrs. showing resonant peaks in frequency. Beam current at 100 μA. Sample temperature +18°C.

The effect of lower beam current (90 μA, adjusted with the electron gun bias control while maintaining the optical probe at the same site) was investigated. (The micro-ammeter reads total current delivered from the electron gun to the anode; only approximately 20 μA of this results in beam current; thus it is estimated that the beam current was reduced by 50% in going from 100 μA to 90 μA.) The frequency spectrum at the lower beam current was markedly distinct from that at the higher current setting, as seen in Figure 3.37. Several of the resonant peaks disappeared entirely, with the highest amplitude peak shifting in frequency from 8.85 to 8.25

Hz. The reduced background noted resulted from a lower overall screen brightness at the lower beam current setting.

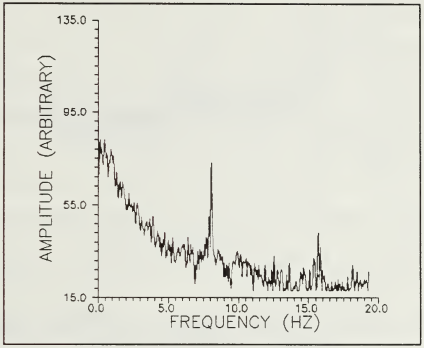

Figure 3.37 Frequency spectrum of sample aged at 450°C for 10 hrs. showing shift in resonant peaks at lower beam current (90 μA). Sample temperature +18°C.

When beam current was returned to the original higher setting of 100 μA, the resonant peaks (at the same site), returned at the same frequencies as the original as seen in Figure 3.38. For example, the highest amplitude peak (8.25 Hz) shifted back to its previous value (8.85 Hz). All resonant peaks returned to their same amplitude within a few percent with the exception of one occurring at 5.25 Hz. This effect of observed frequency shifting when changing system parameters will be discussed in greater detail in the next section.

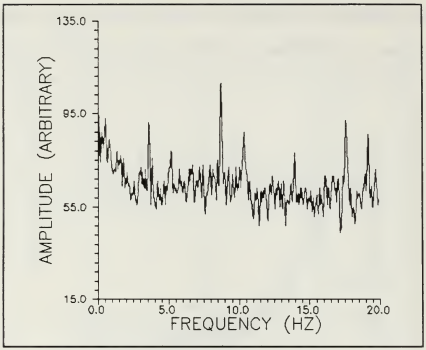

Figure 3.38 Frequency spectrum of sample aged at 450°C for 10 hrs. showing return of resonant peaks as beam current restored to 100 μA. Sample temperature +18°C.

4. The Chaotic Nature of Flicker Motion

The term "chaos" [Ref. 38] is now commonly used when referring to the revolutionary new science which seeks to analyze and unify the behavior of complex systems. Chaos has roots in many scientific disciplines and provides a path of commonality in the modeling of real systems. It becomes possible to model extremely complex processes with very simple mathematical relations.

Certain obvious similarities exist between the present flicker contrast (due to reorientation of small sections of crystal) and the chaotic nature of other physical systems, such as the turbulence often displayed in fluid motion. As

with fluid turbulence, the unpredictable nature of flickering appears to have an underlying order which governs its behavior. The flicker contrast variations observed and described above, and the lattice reorientation from which it arises, display several of the attributes of what is known as chaotic vibration. These characteristics include:

1. Sensitivity of the flickering rate and character to changes in initial conditions.
2. A broadband frequency spectrum as measured by Fast Fourier Transform (FFT) using an electronic spectrum analyzer.
3. Random time evolution trajectories in phase space.
4. Increased complexity of the motion when influenced by changes in system configuration or control parameters (such as sample temperature or electron beam current). This complexity can appear in such effects as sudden period doubling of harmonic frequencies.
5. Nonperiodic bursts of irregular motion.

In connection with the present work, a set of diagnostic tests was performed to determine whether the contrast variations of flicker sites may be characterized as chaotic oscillations. By evaluating the character of the flicker site motion in this way, it was hoped that greater insight could be obtained into the mechanism of the phase

transitions and vibrational damping occurring within the alloy.

A general technique for the rigorous identification of nonperiodic or chaotic motions is given by Moon [Ref. 39], and includes the following checklist:

1. Nonlinear elements in the system should be identified.
2. It should be assured that there are not sources of random input into the system.
3. The real-time history of a measured signal must be observed and analyzed.
4. The phase plane history should be mapped.
5. The frequency spectra of the measured signal should be examined.
6. The effect of variations in system or control parameters ("routes to chaos") should be considered.

Many of the tests for chaotic oscillations are qualitative in nature and involve the judgment and experience of the investigator [Ref. 39]. In the present case, each of the diagnostic checks noted above was examined for its relevance to the behavior of flickering contrast.

a. Nonlinear System Elements.

A necessary condition for chaotic activity is that the system contain nonlinear elements or properties. In a metallic alloy system which undergoes phase transitions such properties might include:

1. Nonlinear damping.
2. Nonlinear boundary conditions.
3. Hysteretic properties of ferromagnetic materials.

The Cu-Mn alloy system displays a specific damping ratio that is a function of the strain (or strain rate) [Ref.

37]. Nonlinear (Coulomb) damping is clearly exhibited, with higher damping capability observed at greater strains. Also, aged Cu-Mn alloys display concentration gradients in the matrix as a result of spinodal decomposition [Ref. 5]. In addition to these differences in elemental concentration, phase boundaries (domains of FCT within the FCC parent matrix) exist in the aged alloy. These properties give rise to discontinuities at the phase or domain boundaries which can effect both the macroscopic damping capability and microscopic flicker activity. It is well-known that FCT Cu-Mn is an anti-ferromagnetic material. One proposed mechanism of its damping capability [Ref. 12] is the anti-ferromagnetic ordering of Mn ions within the matrix.

Non-linearities in a system can also arise in a subtle manner, via the interaction of several properties simultaneously. It can be stated qualitatively that this alloy system displays several properties or features which clearly have nonlinear character, thus meeting this basic requirement for chaotic behavior.

b. Sources of Random Input.

In order to classify a process as chaotic, random excitation must be excluded. Clearly, in these observations of flicker activity, the electron beam energy provides input excitation. In this situation the conclusion that the input energy is deterministic must be approached cautiously, and

correlated with the proposed mechanism which underlies the flicker motion.

If considering only the incident electron beam, it is safe to conclude that this source of excitation is deterministic based on two observed factors: (1) source stability, and (2) source energy spread [Ref. 40]. Modern transmission electron microscopes employ lanthanum hexaboride crystal (LaB_6) filaments which produce steady emission currents (constant emission current over tens of hours within $\pm 2\%$). The influence of energy spread, δE, is proportional to $\delta E/E_o$ where E_o is the accelerating voltage. The energy spread is caused by instabilities in the power supply and by the inherent spread in energies associated with thermionic emission of the electron source. The voltage stability at 100 kV is typically 1 part in 10^6, leading to an energy spread of only 0.1 eV. The energy spread associated with a LaB_6 filament is about 1 eV. Additionally, if significant energy spread is present, image quality will be poor due to chromatic aberration associated with the TEM objective lens.

Inelastic and incoherent scattering of the electron beam as it traverses the sample produces a field of diffuse background energy. This field produces both regular diffraction effects (such as Kikuchi lines) and absorption effects (X-ray and Auger emissions). A broad spectrum of low intensity energies is produced due to varying sample thickness, changes in diffraction condition, and differences

in scattering. Additionally, noise contamination of the input excitation is always present in experimental measurements. As discussed earlier, the energy barrier of flicker motion must be on the order of several tens of electron volts (for the entire section of crystal which reorients). This energy value is able to be supplied by the diffuse background radiation.

The phenomenon of "streaming" [Ref. 31], which has been proposed to be induced by the mechanical vibration of thin sections of a specimen under TEM examination, is likely to be a random process. This conclusion is reached since inelastic scattering developed from randomly distributed thickness contours is the sole source of excitation.

Thus no definite conclusion can be reached that the input source is deterministic, i.e., not random. Other gages of chaotic activity must be employed.

c. Observation of the Time History.

Although this method of identification is not foolproof, observation of a time history record which displays no visible pattern or periodicity can provide a clue that a process is chaotic. (The problem here is that long period behavior is not easily detected and may be periodic.) For example, the time history record of a typical deterministic function (a summation of sine waves) is shown in Figure 3.39, and illustrates the periodic nature of the wave form. On the other hand, the time history record of a typical flicker site,

such as seen in Figure 3.30, shows no periodicity, which is consistent with chaotic oscillation.

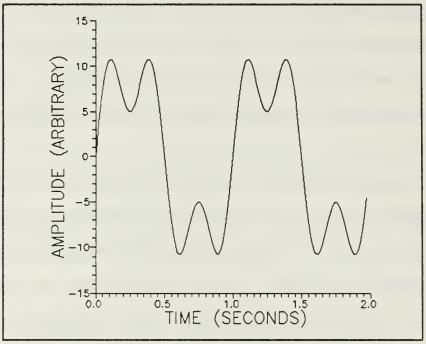

Figure 3.39 Time history record of a deterministic function.

d. Observation of the Phase Space Trajectory.

The phase plane of a system undergoing oscillation displays or graphs one variable (such as displacement) against another (such as velocity). If the oscillation is periodic the phase plane orbit traces a closed curve similar to those pictured in Figures 3.40 and 3.41. (Forced nonlinear systems display phase plane orbits which cross, but the orbit is still closed.) Chaotic motions, however, have phase plane orbits which never close or repeat. The trajectory of these orbits tends to fill a section of the plane.

If only one parameter is measured (as in our case) a pseudo-phase plane map can be employed. In this technique a plot of one variable is made versus itself but delayed or advanced by a fixed time constant: [x(t), x(t+τ)]. The selection of the time delay τ is not critical and can be achieved using various computer generated data techniques. The effect of altering the time constant is to open up or close the orbit of the pseudo-phase plane plot as illustrated below in Figures 3.40 and 3.41.

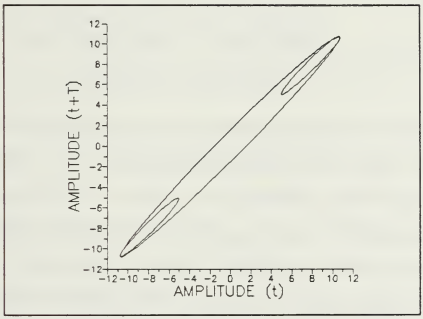

Figure 3.40 Pseudo-phase plane history of periodic function illustrating effect of adjusting time delay τ. Short time delay.

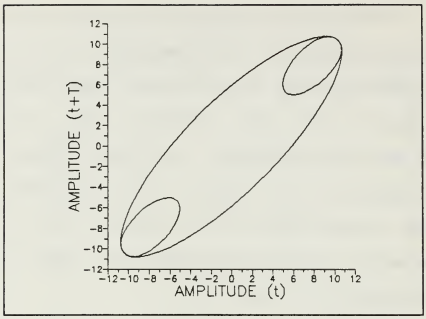

Figure 3.41 Pseudo-phase plane history of periodic function illustrating effect of adjusting time delay τ. Long time delay.

In the present analysis, data from a typical time history record of a flicker site was stored digitally [Ref. 41], and electronically delayed for 17 milliseconds. The flicker contrast intensity at time t was plotted versus intensity at time $(t + \tau)$. The pseudo-phase plane map which results is shown in Figure 3.42. The path is obviously confined, yet is wandering, but aside from the fact that this is consistent with chaotic behavior, it does not provide an indication of the underlying physical process. Appendix C contains the computer programs used to produce the time delays in the intensity data.

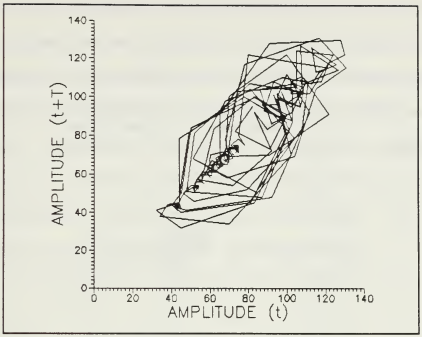

Figure 3.42 Pseudo-phase plane history of flicker intensity. (17 millisecond electronically produced time delay.)

An extension of this technique can be used to show the presence of a "strange attractor" in phase space. A strange attractor is a locus in phase space to which the data is restricted, but on which the sequence of appearance of the data points is unpredictable. In essence, an attractor, if present (and if detected), defines an underlying "order" or "connectivity" between the apparently unrelated sequence of events in the observed behavior. In the present case of flickering contrast in TEM images, such an attractor was eventually revealed by creating a phase space composed of the difference in intensity over one time interval plotted against the difference in intensity in the adjacent time interval, as

seen in Figure 3.43. Although the resolution of this plot is limited, a possible fractal quality is evident. The result is markedly different from that produced by a random data set.

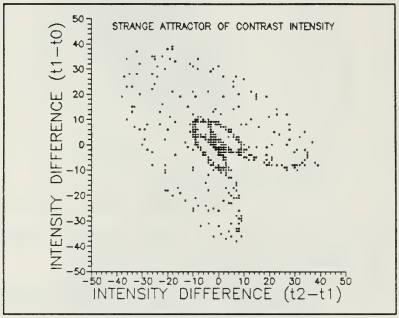

Figure 3.43 Pseudo-phase plane history of flicker intensity showing the presence of a "strange attractor".

e. Examination of Frequency Spectrum.

Another clue to the presence of chaotic activity is a broadband spectrum of frequencies in the output signal. This technique must also be cautiously applied in our analysis since the system is assumed to have many degrees of freedom. (This characteristic identifier of chaotic activity is more relevant in a system of low dimension.) In large degree-of-freedom systems such as our solid crystalline model, a broad frequency spectrum can still be used to detect chaotic

behavior. This can be achieved by the observation of changes in the spectrum as we vary some parameter such as sample temperature or electron beam current. Figure 3.44 illustrates the frequency spectrum of a deterministic system, and is provided for comparison with the frequency spectra shown earlier, which were obtained by monitoring flicker sites. The spectra obtained from flicker activity all show a characteristic broadband range of frequencies.

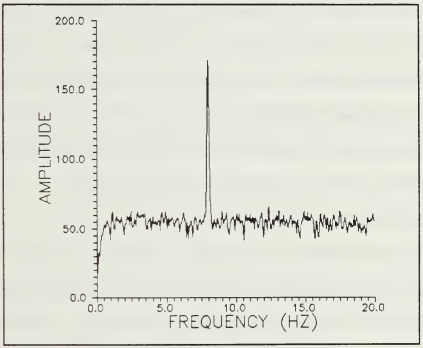

Figure 3.44 Frequency spectrum of periodic system. Spike occurring at 8 Hz is the fundamental frequency of system. Broadband spectrum of low amplitude is typical of noise picked up in sensor. (Spectrum produced with signal from pure 8 Hz sine wave with 50 Hz bandwidth noise injected for comparison.)

f. Varying System Parameters ("Routes to Chaos").

Another test used to identify chaotic oscillations is to examine changes in system output as one or more control parameters are varied. This test looks for patterns of periodic responses (such as the appearance of sub-harmonics) as a particular system parameter is changed. In the present case, two control parameters were varied while examining flicker activity in the TEM, namely specimen temperature and electron beam current. The effect of changes in electron beam intensity on flicker activity was even more pronounced than the temperature effect. As seen earlier (Figures 3.36 through 3.38) the characteristic resonant peaks died out as beam current was reduced (some resonant peaks shifted in frequency) and returned as beam current was restored.

5. Mechanism of Flicker Activity

The kinematics of small sections of the crystalline lattice of an aged Cu-Mn-Al damping alloy under electron beam irradiation have been examined in detail. This examination has provided insight as to the underlying physical mechanism of the contrast variation and can be correlated to the alloy's high damping behavior.

Several of the "small-clusters" studies mentioned earlier considered structural changes within groups of atoms isolated from the influence of a suspending matrix. However, a similar situation can be implied for the present case, where small crystallographic domains comprise zones in which

incipient transition of an FCT structure may occur. These domains oscillate in orientation as they exist within the parent matrix and as they maintain communication with one another. Electron beam heating as the sole cause of the crystallographic oscillation can probably be excluded, as can any diffusional or electrostatic effect. However, the energy barrier of flicker motion must be of the same order of magnitude as the effects described in the "small-cluster" studies, namely several tens of electron volts.

Changes in electron beam intensity markedly affects the flicker activity. The source of energy (when examined in the TEM) is likely to be the diffuse energy background present as a result of inelastic scattering of the electron beam within the sample. Local stresses which arise due to temperature gradients are in competition with the lattice stresses which are induced by concentration gradients resulting from aging. The result of this competition is the random and time dependent oscillation in FCT orientation which we observe.

It should be noted that the "streaming" effect described earlier has some significant distinctions from that of the flicker motion observed in the present study. Flicker motion could be seen only in aged samples and was readily observed in specimens of constant thickness with no bend contours. Additionally, the flicker motion continued as long as it was being irradiated by the electron beam.

Several investigators have previously described the local premartensitic instability of the FCC phase in Cu-Mn alloys and have indicated that such structure changes approach the behavior of second-order transitions [Ref. 15, 42]. This conclusion is supported by the present research, in that close examination of the time-domain history of intensity change reveals a relatively gradual transition from dark to bright contrast. The gradual contrast variation implies that the underlying structural change is also not instantaneous, but gradual, and therefore consistent with a second-order transition.

Since the quantitative magnitude of flicker activity correlates with variations in the alloy's damping capacity, the mechanism of flicker activity must also be influenced by elastic strain energy. Macroscopic vibrational energy is stored and dissipated by the internal microscopic reorientation of small regions of the crystal lattice. The result is a damping mechanism.

C. TRANSFORMATION MODEL FOR AGED ALLOYS

Here is presented a model, on a scale somewhat greater than the atomistic level, of the morphology of structures developed during aging and subsequent cooling of Cu-Mn alloys. This model leads to an explanation of how flickering activity, which corresponds to oscillations in the orientation of tetragonal sections of crystal, can occur upon electron beam irradiation during TEM examination.

Manganese rich Cu-Mn alloys have been shown to undergo decomposition at elevated temperatures [Ref. 5, 15]. This decomposition, which occurs within the miscibility gap of the Cu-Mn phase diagram, leads to a segregation of Mn-enriched and Mn-depleted regions [Ref. 4]. Additionally, a diffusionless transformation from FCC to FCT occurs within the Mn-enriched regions upon cooling from aging temperature [Ref. 7]. The temperature at which the FCC-FCT transformation occurs is closely associated with the Néel temperature [Ref. 43]. What results is, in effect, a co-modulation of structure and composition, similar to that diagrammed in Figure 3.46. The effect of varying the aging conditions is to alter the amplitude and wavelength of the composition gradient. The wavelength of the modulation is postulated to be on the order of the striations of tweed contrast observed in the aged alloys, namely 10 to 20 nm. Additionally, the wavelength of composition modulation is likely to increase with aging.

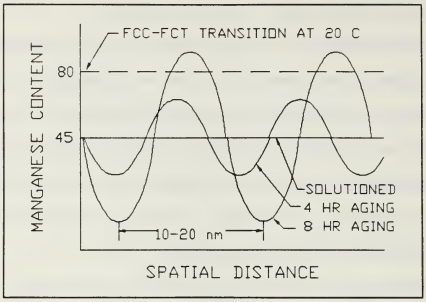

Figure 3.46 Composition modulation occurring in aged Cu-Mn alloys showing variation of with aging conditions. FCC-to-FCT transition at 20°C shown as dashed line. The wavelength of the composition gradient is on the order of the tweed striations (10 to 20 nm).

Since the M_s is a function of manganese content, a certain dispersion of transformation-prone regions are created by a given aging treatment. In these Mn-enriched regions, conditions are favored for the nucleation of the FCT structure upon cooling. The formation of this FCT "martensite" becomes more favored as the "core" of the Mn-enriched region (i.e., the peak of the composition wave of Figure 3.46) is approached, and as the specimen temperature is lowered. This in effect, produces a continuous gradient of parent phase instability. This is consistent with TEM observations, in which we see that the FCC-to-FCT transition is entirely coherent. As aging progresses, the peak Mn enrichment

increases, which enhances the ability to nucleate martensite during cooling.

The regions of tetragonality (within the regions of Mn enrichment) develop in the form of very thin platelets (or pseudo-platelets) with the thin dimension lying parallel to <111> directions of the parent FCC matrix. The matrix strain produced by these disk-shaped platelets is a composite of the misfit strain due to the Mn enrichment and the tetragonality of the nucleated FCT martensite. The elastic strain field produced by these FCT platelets is aligned with the <111> directions of the parent FCC matrix. It seems likely that these platelets form interactive sets (with members on various (111) planes) within a small region of the matrix, with the strain fields of the individual platelets superimposed on one another.

The thin disk-shaped platelets have not been detected directly by TEM observation. Their presence is inferred by the diffuse streaking visible in the diffraction patterns of relatively longer aged Cu-Mn alloy samples. Detailed analysis of the streak directions indicates that the platelets are very thin, and the thin dimension lies normal to <111> directions of the FCC matrix.

Within the gradient of composition (with accompanying gradient in M_s) there must also exist a gradual transition to tetragonality. This can be thought of on two scales. First, there must exist a gradient of tetragonality associated with

the nucleated martensite within the Mn-enriched regions, and second, there apparently exists a gradient of tetragonal distortion of a larger region of surrounding crystal, whose distortion to FCT arises from the composite strains of a group of platelets. The distortion of this larger region of crystal, which we will refer to as a "strained region of crystal" (SRC), is closely coupled with the net strain in adjoining "strained regions of crystal". The variation of the orientation of the tetragonal c-axis within the SRCs leads to the contrast observed as V-shaped images in TEM examination.

A model of a "strained region of crystal" can be created in order to explain the oscillation in orientation of the tetragonal c-axis within that region, an effect which comprises the flicker event. Referring to Figure 3.47, an array of "quasi-platelets" is depicted within the volume of the SRC. The nucleated platelets lie on {111} planes of the FCC "parent" matrix. Stress arising from misfit and martensitic transformation of these platelets establishes a net tensile stress field within the SRC. As the composite stress increases due to the influence of composition, temperature, and external stress, the SRC can undergo a "relaxation" where by the net <111> directions of the SRC elongate. This effectively shifts the original FCC SRC toward a FCT structure. Again it must be emphasized that this transition is gradual, obtaining a higher degree of tetragonality as the core of the SRC is approached. One SRC

region can thus trigger or influence the shifting of its neighbors in a self-accommodating manner.

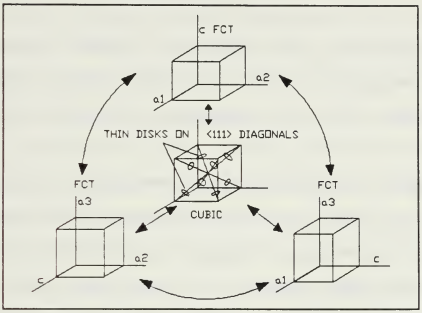

Figure 3.47 Three dimensional model of strained region of crystal showing three possible FCT orientations. Two transformation "paths" are depicted; 1, FCT-to-FCC-to-FCT, and 2, direct FCT-to-FCT.

In this model, the transition of a given SRC from one c-axis orientation to another can occur in two ways. The SRC can either undergo a FCT-to-FCC-to-FCT reaction in the process of re-orienting the tetragonal c-axis, or can undergo a "direct" FCT-to-FCT transition. Using an energy path approach to determine which transition is favored, it is obvious that the direct FCT-to-FCT transition (a change of the SRC from one tetragonal c-axis orientation to another without passing through a cubic intermediate state) requires less energy. (This approach assumes a constant volume SRC.)

VI. CONCLUSIONS

A comparison of predicted versus actual V-image extinctions indicates that a "global" static distortion, **R**, of the form <111>, is present. The exact mechanism of development of this global matrix distortion is as yet unknown, but is apparently a composite of the distortions produced by a set of the thin tetragonal platelets.

Diffuse streaking of both the transmitted and diffracted spots of the SADP indicate the presence of thin disc-shaped regions of a second phase. The thin discs or platelets lie with normals in <111> directions of the parent phase and are coherent within the matrix. The streaks are observed over a broad range of specimen orientation and indicate that the discs are very thin (on the order of several tens of nm at the most).

Samples aged for shorter times, which display tweed, show no evidence of streaks at the 000 spot, indicating that the incipient transformation of the platelets has not yet occurred or is below a threshold of detection.

Conditions for the establishment of the dispersed regions (in the form of thin discs) are created by the decomposition of the parent FCC matrix. A fine-scale composition modulation of the microstructure develops during aging which

establishes a continuous gradient of parent phase lattice instability.

The V-shaped image contrast arises from the strain field of the distorted matrix, not from a direct image projection of the habit or shape of the platelets. (Projections of the platelets would produce images which do not fit the extinction analysis.)

The dynamic nature ("flickering") of the V-shaped images results from the instability of small tetragonally-distorted regions of crystal which develop within the composition gradient of the parent phase. The energy supplied during the electron beam irradiation of TEM examination overcomes the relatively small energy barrier for reorientation of the FCT c-axis. It is apparent that a direct FCT-to-FCT mechanism of reorientation of the tetragonality is favored, and that this transition occurs gradually both in time and distance.

Variations in diffraction contrast (flickering) in an aged Cu-Mn-Al alloy are associated with the kinematic reorientation of small sections of the crystalline lattice. The motion thus defined can be used to further explain the underlying mechanism which produces the contrast variation.

Real-time behavior of the contrast variation at individual flicker sites suggests that the underlying mechanism which produces the contrast change is a gradual crystallographic transition, such as would be typical of a second-order phase transition, and supports previous work on this alloy system.

The exact character of contrast variation at individual flicker sites is influenced by specimen temperature and by the extent of electron beam irradiation. The diffuse background energy supplied by inelastic scattering of the electron beam within the sample probably provides the source of excitation.

The phenomenon of resonance in the process of tetragonal reorientation may indicate that an array of small tetragonal regions of the crystal are coupled through the parent matrix. The intervening matrix regions, having lower degrees-of-freedom, allow oscillation at relatively few fundamental frequencies.

The contrast variations at individual flicker sites display certain qualities similar to turbulence in fluid motion. The underlying physical processes are chaotic and not predictable.

V. RECOMMENDATIONS FOR FUTURE STUDY

The following recommendations for futher research are provided:

Develop additional crystallographic models (or validate existing models) to define the changes which occur during aging and the dynamic effect of flickering.

Use the models in conjunction with available computer graphics routines (PATRAN - NASTRAN) to simulate the dynamics of the lattice transitions which occur.

Develop mathematical equations of strain fields in the matrix to use in conjunction with computer-generated electron micrograph simulations of tweed and flicker sites.

Use other techniques of monitoring the phase transitions. (Automate data acquisition of resistivity vs. time/temperature or specific heat capacity vs. time/temperature.)

Investigate other martensitic/shape memory alloys for evidence of flickering or other dynamic behavior.

Investigate time and frequency domain characteristics of shimmering effect reported by Otsuka and Wayman [Ref. 31].

APPENDIX A

CONSTRUCTION OF IMAGE CONVERTER

The fiber optic image converter used to read image intensity from the TEM video screen was constructed from a kit developed by the ADVANCED FIBEROPTICS CORPORATION. The EDU-LINK$_{TM}$ Fiber Optic Kit package contained 2 pre-designed printed circuit boards and all necessary components. Although both a transmitter and receiver were supplied in the kit, only the receiver portion was used in this project. Table A.1 contains the parts list for both transmitter and receiver.

TABLE A.1 PARTS LIST FOR FIBER OPTIC IMAGE CONVERTER

PARTS LIST

TRANSMITTER			RECEIVER		
		color code			color code
U1	CD4093BE	QUAD CMOS NAND	U1	LM324N	QUAD OP AMP
Q1	2N3904 or 2N4401	NPN TRANSISTORS	Q1	2N3904 or 2N4401	NPN TRANSISTORS
R1	75 ohm	violet green black	R1	200 Kohm	red black yellow
R2	3.9 Kohm	orange white red	R2,R5,R6	4.7 Kohm	yellow violet red
R3,R4	30 Kohm	orange black orange	R3,R4	47 Kohm	yellow violet orange
R5	300 Kohm	orange black yellow	C1	0.1 uf	CAPACITORS
R6	4.7 Kohm	yellow violet red			
C1	.01 uf	CAPACITORS	D1	MRD721	MOTOROLA
D1	CVQ-20-3	SIEMANS LED			DETECTOR

The receiver employs a newly designed PIN photodiode with a 0.2 microamp/microwatt responsivity and a 1 nanosecond rise time. Details of the printed circuit board and receiver schematic are presented in Figures A.1 and A.2.

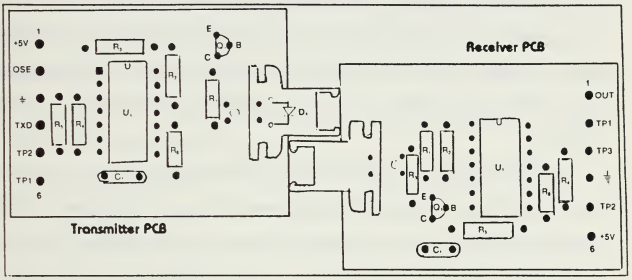

Figure A.1 Fiber optic image converter circuit board.

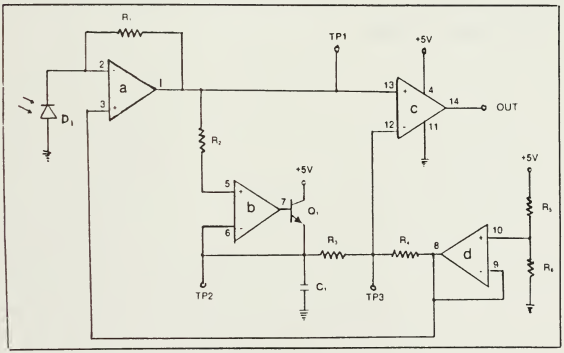

Figure A.2 Fiber optic image converter schematic.

APPENDIX B

HOW TO VIEW STEREOGRAPHIC IMAGES

The stereographic image pairs presented in this thesis can be viewed without the aid of a stereoscope using a technique called free-fusion. With this technique, each eye focuses on its respective image until the pictures merge into a single image.

To perform this technique, bring the image pair right up to your face, almost touching your nose, and concentrate on some prominent part of the picture. Then slowly move the pictures out to a distance where they appear in focus. Observe what now appears to be the middle of the three side-by-side images. A three-dimensional effect will be present in the center image.

APPENDIX C

COMPUTER PROGRAMS

This appendix contains the BASIC computer programs used manipulate the data from the spectrum analyzer to produce the pseudo-phase space plots contained in this thesis. The programs use the data files produced by the Signal Analyzer Interface Program [Ref. 41].

The first program was used to produce the data points for the pseudo-phase space map shown in Figure 3.42. The second program produced the data points which identified the "strange attractor" of Figure 3.43.

```
100  REM  PROGRAM TO CONVERT TIME HISTORY RECORD TO PSEUDO-
110  REM  PHASE SPACE MAP.
115  DIM  Q(255), X(255), Y(255)
120  CLS
130  PRINT "PSEUDO-PHASE SPACE MAP DATA CONVERSION PROGRAM"
140  PRINT "FILES "*.OUT"
150  INPUT "INPUT FILE NAME";FILE1$
160  INPUT "OUTPUT FILE NAME";FILE2$
170  OPEN  "C:\MATH\BASIC\" + FILE1$ FOR INPUT AS #1
180  OPEN  "C:\MATH\GRAPHER\" + FILE2$ FOR OUTPUT AS #2
190  FOR N = 1 TO 250
200      INPUT#1, Q(N), X(N), Y(N)
210  NEXT N
220  FOR M = 1 TO 250
230      PRINT#2, M; Y(M), Y(M+1)
240  NEXT M
250  PRINT "DATA CONVERSION COMPLETE"
260  END
```

```
100  REM  PROGRAM TO COMPUTE INTENSITY DIFFERENCES TO ALLOW
110  REM  PLOTTING OF PHASE SPACE DATA (STRANGE ATTRACTOR)
120  CLS
130  PRINT "PSEUDO-PHASE SPACE MAP DATA CONVERSION PROGRAM"
135  PRINT "TO REVEAL THE PRESENCE OF A STRANGE ATTRACTOR"
140  PRINT "FILES "*.OUT"
150  INPUT "INPUT FILE NAME";FILE1$
160  INPUT "OUTPUT FILE NAME";FILE2$
170  OPEN  "C:\MATH\BASIC\" + FILE1$ FOR INPUT AS #1
180  OPEN  "C:\MATH\GRAPHER\" + FILE2$ FOR OUTPUT AS #2
190  INPUT "ENTER MAX DATA POINTS"; NMAX
200  DIM N(500), X(500), Y(500), XX(500), YY(500)
210  FOR I = 1 TO NMAX
220      INPUT#1, N(I), X(I), Y(I)
230  NEXT I
240  Y(0)=Y(1)
250  FOR J = 1 TO NMAX
260      XX(J) = Y(J+1) - Y(J)
270      YY(J) = Y(J)   - Y(J-1)
280      PRINT    J, XX(J), YY(J)
290      PRINT#2, J, XX(J), YY(J)
300  NEXT J
310  PRINT "DATA CONVERSION COMPLETE"
320  END
```

VI. REFERENCES

1. Harris, C. M. and others, Shock and Vibration Handbook, McGraw-Hill Book Co., 1988.

2. Schetky, L. M. and Perkins, A. J., "The 'Quiet' Alloys", Machine Design, pp. 202-206, April 1978.

3. Mayes, L. L., An Electron Microscopy Study of Tweed Microstructures and Premartensitic Effects in a High Damping 53Cu-45Mn-2Al Alloy, M. S. Thesis, Naval Postgraduate School, Monterey, CA, March 1988.

4. Vitek, J. M. and Warlimont, H., "On a Metastable Miscibility Gap in Gamma-Mn-Cu Alloys and the Origin of their High Damping Capacity", Metal Science, Vol. 10, No. 1, pp. 7-13, 1976.

5. Vintaykin, Ye. Z., Dmitriyev, V. B. and Udovenko, V. A., "Spinodal Decomposition in Manganese-Copper Alloys", Physical Metallurgy and Metallography, Vol. 46, No. 4, pp. 97-107, 1978.

6. Basinski, Z. S. and Christian, J. W., "The Cubic-Tetragonal Transformation in Manganese-Copper Alloys", Journal of the Institute of Metals, Vol. 80, pp. 659-666, 1951-52.

7. Bichinashvili, A. I., Vintaykin, Ye. Z., Litvin, D. F. and Udovenko, V. A., "X-ray Investigation of the FCC-to-FCT Transformation in Manganese-Copper Alloys", Physical Metallurgy and Metallography (in Russian, Fiz. Metal. Metalloved.), Vol. 41, No. 1, pp. 112-117, 1976.

8. Meneghetti, D. and Sidhu, S. S., "Magnetic Structures in Copper-Manganese Alloys", Physical Review, Vol. 105, No. 1, pp. 130-135, 1957.

9. Bacon, G. E., Dunmur, I. W., Smith J. H. and Street R., "The Antiferromagnetism of Manganese Copper Alloys", Proceedings of the Royal Society of London, Series A, Vol. 241, pp. 223-238, 1957.

10. Makhurane, P. and Gaunt, P., "Lattice Distortion, Elasticity and Antiferromagnetic Order in Copper-Manganese Alloys", Journal of Physics C: Solid State Physics, Ser. 2, Vol. 2, pp. 959-965, 1969.

11. Basinski, Z. S. and Christian, J. W., "The Cubic-Tetragonal Transformation in Manganese-Copper Alloys", Journal of the Institute of Metals, Vol 80, pp. 659-666, 1951-52.

12. Hedley, J. A., "The Mechanism of Damping in Manganese-Copper Alloys", Metal Science Journal, Vol. 2, pp. 129-137, 1968.

13. Nittono, O., Satoh, T. and Koyama Y., "Cubic-Tetragonal Transformation and Reversible Shape Memory Effect in Manganese-Copper Alloys", Transactions of the Japan Institute of Metals, Vol. 22, No. 4, pp. 225-236, 1981.

14. Cowlan, N., Bacon, G. E. and Gillott, L., "Changes in Cell Dimensions at the Martensitic Transformation in Gamma Mn-Cu Alloys", Journal of Physics F: Metal Physics, Vol. 7, No. 12, pp. L315-L319, 1977.

15. Vintaykin, Ye. Z. and Udovenko, V. A., "Premartensite Instabilities in Manganese-Copper Alloys", Physical Metallurgy and Metallography (in Russian, Fiz. Metal. Metalloved.), Vol. 51, No. 5, pp. 160-162, 1981.

16. Butler, E. P. and Kelly, P. M., "High Damping Capacity Manganese-Copper Alloys. Part 1 - Metallography", Transactions of the Metallurgical Society of AIME, Vol. 242, pp. 2099-2106, 1968.

17. Shimizu, K., Okomura, Y. and Kubo, H.,"Crystallographic and Morphological Studies on the FCT-to-FCT Transformation in Mn-Cu Alloys", Transactions of the Japan Institute of Metals, Vol. 23, No. 2, pp. 53-59, 1982.

18. Tanner, L. E., "Diffraction Contrast from Elastic Shear Strains due to Coherent Phases", Philosophical Magazine, Vol. 14, No. 127, p. 111-130, 1966.

19. Robertson, I. M. and Wayman, C. M., "Tweed Microstructures: I. Characterization of Beta-NiAl", Philosophical Magazine A, Vol. 48, No. 3, pp. 421-442, 1983.

20. Delaey, L., Perkins, A. J. and Massalski, T. B., "Review: On the Structure and Microstructure of Quenched Beta-Brass Type Alloys", Journal of Materials Science, Vol. 7, pp. 1197-1215, 1972.

21. Tanner, L. E., "The Ordering Transformation in Ni_2V", Acta Metallurgica, Vol. 20, pp. 1197-1227, 1972.

22. Schryvers, D., Tanner, L. E. and Tendeloo, G. V., "Premartensitic Microstructures as Seen in the High Resolution Electron Microscope: A Study of a Ni-Al Alloy", NATO/ASI Symposium on Phase Stablity, Crete, June 1984, A. Gonis and M. Stocks Editors (Martinus Nijhoff Publishing, Dordrecht, Netherlands), 1988.

23. Perkins, A. J., Mayes, L. L. and Yamashita, T., "Flickering Contrast in TEM Images of Tweed Microstructures in an Aged Cu-Mn-Al Alloy," Scripta Metallurgica, Vol. 22, No. 6, pp 887-892, 1988.

24. Perkins, A. J., Mayes, L. L. and Yamashita, T., "Effects of Aging on the Morphology of Flickering Contrast in Tweed Microstructures of Cu-Mn-Based Alloys," Scripta Metallurgica, Vol. 22, No. 7, pp. 1137-1142, 1988.

25. Perkins, A. J., "Tweed Microstructures and the Evolution of Damping in Cu-Mn Based Alloys", Phase Transformations '87, The Institute of Metals, London, pp. 165-168, 1988.

26. Iijima, S. and Ichihashi, T., "Structural Instability of Ultrafine Particles of Metals", Physical Review Letters, Vol. 56, No. 6, pp. 616-619, February 1986.

27. Smith, D. J., Petford-Long, A. K., Wallenberg, L. R. and Bovin, J. O., "Dynamic Atomic-Level Rearrangements in Small Gold Particles", Science, Vol. 233, pp. 872-875, August 1986.

28. Bovin, J. O., Wallenberg, L. R. and Smith, D. J., "Imaging of Atomic Clouds Outside the Surfaces of Gold Crystals by Electron Microscopy", Nature, Vol 317, pp. 47-49, September 1985.

29. Marks, L. D., Ajayan, P. M. and Dundurs, J., Ultramicroscopy, Vol. 20, 1986.

30. Dundurs, J., Marks, L. D. and Ajayan, P. M., "Structural Fluctuations in Small Particles", Philosophical Magazine A, Vol. 57, No. 4, pp. 605-620, 1988.

31. Otsuka, K., Kubo, H. and Wayman, C. M., "Diffuse Electron Scattering and 'Streaming' Effects", Metallurgical Transactions A, Vol. 12A, pp. 595-605, 1981.

32. Birchon, D., Bromley, D. E. and Healey, D., "Mechanism of Energy Dissipation in High-Damping-Capacity Manganese-Copper Alloys", Metal Science Journal, Vol. 2, pp. 41-46, 1968.

33. Oshima, R., Sugiyama, M. and Fujita, F. E., "Tweed Structures Associated with FCC-FCT Transformations in Fe-Pd Alloys", Metallurgical Transactions A, Vol. 19A, pp. 803-810, 1988.

34. Van Tendeloo, G., Chandrasekaran, M. and Lovey, F. C., "Modulated Microstructures in Beta Cu-Zn-Al", Metallurgical Transactions A, Vol 17A, pp. 2153-2161, 1986.

35. Edington, J. W., Practical Electron Microscopy in Materials Science, Van Nostrand Reinhold Company, 1976.

36. Hirsch, P. B., Howie, A., Nicholson, R. B., Pashley, D. W. and Whelan, M. J., Electron Microscopy of Thin Crystals, The Butterworth Group, 1971.

37. Reskusich, J. and Perkins, A. J., "Damping Behavior of Incramute: Strain Dependence and Heat Treatment Effects", Naval Postgraduate School Technical Report No. NPS 69-87-001, Monterey, CA, September 1986.

38. Gleick, J., Chaos: Making a New Science, Viking Penguin Inc., 1987.

39. Moon, F. C., Chaotic Vibrations, An introduction for Applied Scientists and Engineers, John Wiley & Sons, 1987.

40. Loretto, M. H., Electron Beam Analysis of Materials, Chapman and Hall, 1984.

41. Patch, G. R., Development of a Data Acquisition and Analysis System for High Damping Alloy Evaluation, M. S. Thesis, Naval Postgraduate School, Monterey, CA, 1987.

42. Vintaykin, Ye. Z., Udovenko, V. A., Litvin, D. F. and Serebryakov, V. G., "Elastic Constants of Manganese-Copper Alloys", Physical Metallurgy and Metallography (in Russian, Fiz. Metal. Metalloved.), Vol. 49, No. 4, pp. 182-185, 1980.

43. Smith, J. H. and Vance, E. R., "Decompostion of Gamma-Phase Manganese Copper Alloys", Journal of Applied Physics, Vol. 40, No. 12, pp. 4853-4858, 1969.

INITIAL DISTRIBUTION LIST

		No. Copies
1.	Defense Technical Information Center Cameron Station Alexandria, Virginia 22304-6145	2
2.	Library, Code 0142 Naval Postgraduate School Monterey, California 93943-5002	2
3.	Professor Jeff Perkins, Code 69 Ps Department of Mechanical Engineering Naval Postgraduate School Monterey, California 93943-5004	6
4.	LCDR D. M. Farkas Mare Island Naval Shipyard Vallejo, California 94592-5100	2
5.	Mrs. Catherine Wong, Code 2812 David Taylor Naval Ship R & D Center Annapolis, Maryland 21402	3
6.	Mr. Robert Hardy, Code 2803 David Taylor Naval Ship R & D Center Annapolis, Maryland 21402	3
7.	Dean of Science and Engineering, Code 06 Naval Postgraduate School Monterey, California 93943-5000	1
8.	Research Administration, Code 012 Naval Postgraduate School Monterey, California 93943-5000	1
9.	Department Chairman, Code 69 Hy Department of Mechanical Engineering Naval Postgraduate School Monterey, California 93943-5004	1
10.	Professor Y. S. Shin, Code 69 Sg Department of Mechanical Engineering Naval Postgraduate School Monterey, California 93943-5000	1

11. Mr. Charles Zanis, Code 196 — 1
Naval Sea Systems Command
Washington D.C. 20352-5101

12. Lcdr Wallace M. Elger, Code 05MB — 1
Naval Sea Systems Command
Washington D.C. 20362-5101

13. Mr. A. G. S. Morton, Code 2813 — 1
David Taylor Naval R & D Center
Annapolis, Maryland 21402

14. Mr. V. J. Castelli, Code 2844 — 1
David W. Taylor Research Center
Annapolis, Maryland 21402

Thesis
F2254
c.1

Farkas
A microstructural investigation of the shear distortions and energetics of motions observed in an aged high damping 53-Cu-45Mn-2Al alloy.

Thesis
F2254
c.1

Farkas
A microstructural investigation of the shear distortions and energetics of motions observed in an aged high damping 53-Cu-45Mn-2Al alloy.

thesis2284
A microstructural investigation of the s
3 2768 000 81764 7
DUDLEY KNOX LIBRARY